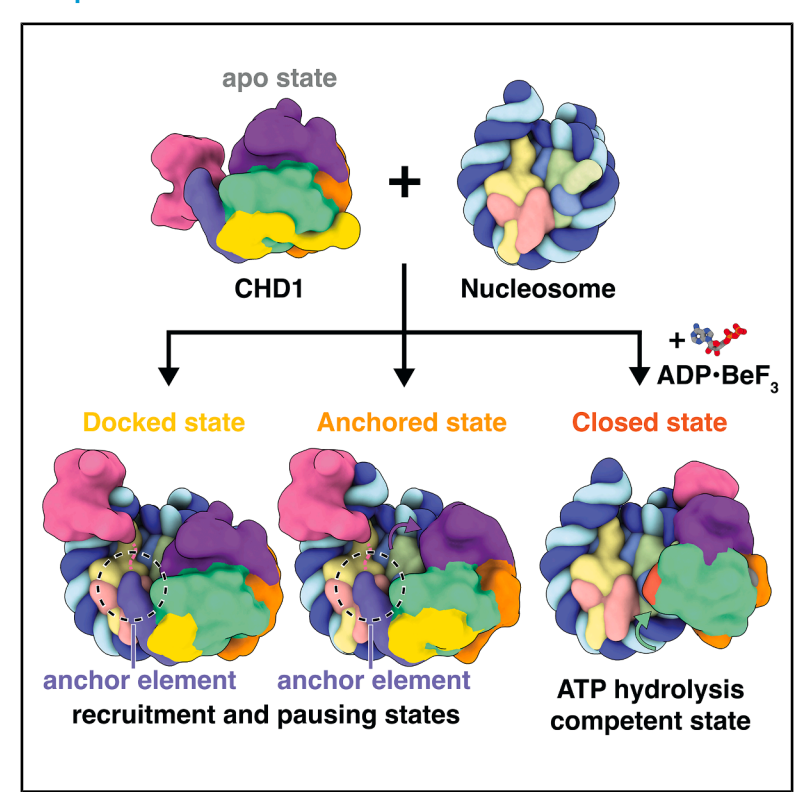
# Structural basis of human CHD1 nucleosome recruitment and pausing

### **Graphical abstract**



### **Authors**

Allison M. James, Lucas Farnung

### Correspondence

lucas\_farnung@hms.harvard.edu

### In brief

James and Farnung identify three structural snapshots of CHD1-nucleosome complexes, visualizing conserved regulatory elements that explain how CHD1 binds nucleosomes, senses DNA, and controls remodeling directionality. Their work provides a mechanistic model for how chromatin remodelers couple nucleosomal substrate recognition to directional nucleosome sliding activity.

### **Highlights**

- Cryo-EM structures capture human CHD1 recruitment and pausing snapshots
- CHD1 DNA-binding region binds entry-side DNA to direct remodeling
- CHD1 anchor element tethers ATPase motor to the nucleosome acidic patch
- Conformational switch in the CHD1 gating element is crucial for nucleosome sliding







### **Article**

# Structural basis of human CHD1 nucleosome recruitment and pausing

Allison M. James<sup>1</sup> and Lucas Farnung<sup>1,2,\*</sup>

<sup>1</sup>Department of Cell Biology, Blavatnik Institute, Harvard Medical School, Boston, MA 02115, USA

<sup>2</sup>Lead contact

\*Correspondence: lucas\_farnung@hms.harvard.edu https://doi.org/10.1016/j.molcel.2025.04.020

### SUMMARY

Chromatin remodelers regulate gene expression and genome maintenance by controlling nucleosome positioning, but the structural basis for their regulated and directional activity remains poorly understood. Here, we present three cryoelectron microscopy (cryo-EM) structures of human chromodomain helicase DNA-binding protein 1 (CHD1) bound to nucleosomes that reveal previously unobserved recruitment and regulatory states. We identify a structural element, termed the "anchor element," that connects the CHD1 ATPase motor to the nucleosome entry-side acidic patch. The anchor element coordinates with other regulatory modules, including the gating element, which undergoes a conformational switch critical for remodeling. Our structures demonstrate how the DNA-binding region of CHD1 binds entry- and exit-side DNA during remodeling to achieve directional sliding. The observed structural elements are conserved across chromatin remodelers, suggesting a unified mechanism for nucleosome recognition and remodeling. Our findings show how chromatin remodelers couple nucleosome recruitment to regulated DNA translocation, providing a framework for understanding chromatin remodeler mechanisms beyond DNA translocation.

### INTRODUCTION

Chromatin remodeling governs DNA accessibility in eukaryotes,<sup>1</sup> orchestrating fundamental biological processes such as gene expression, DNA replication, and DNA repair.<sup>2</sup> To translocate DNA, chromatin remodelers oscillate between open and closed states of their ATPase motor and thereby induce specific geometric changes via a DNA twist diffusion-based mechanism.<sup>4,5</sup> However, this oscillation alone does not explain how remodelers achieve the directional and regulated chromatin remodeling observed in vitro and in vivo. 6-11 Remodelers exhibit distinct periods of interspersed pausing between multi-base pair bursts of remodeling, 4,11,12 which are hypothesized to serve as regulatory checkpoints, allowing the remodelers to sense entry- and exitside DNA to achieve a directional remodeling outcome. Auxiliary elements of the chromatin remodeler and interactions with nucleosomal features such as the H2A-H2B acidic patch have been implicated in regulating the recruitment to nucleosomes and sensing of DNA during pausing. 6,7,10,11,13,14

The evolutionary conserved human chromatin remodeler chromodomain helicase DNA-binding protein 1 (CHD1) is involved in transcription regulation 15,16 and DNA repair 17,18 and is a tumor suppressor in prostate cancers. 19 Like other CHD family members, *H. sapiens* CHD1 slides nucleosomes. CHD1 contains several auxiliary domains flanking the ATPase motor. These include an autoregulatory N-terminal double chromodomain that binds to trimethylated histone H3 residue lysine 4 (H3K4me3)<sup>20</sup>

and a C-terminal DNA-binding region (DBR) that senses the entryand exit-side DNA.<sup>21</sup> Additional regulatory motifs, such as the bridge and the guide-strand-displaced (GSD) helix, are part of a NegC-like region and play a key role in coordinating DNA translocation and entry-side DNA sensing. Together with an element in the ATPase motor termed the "gating helix,"<sup>3,22</sup> the bridge and GSD helix are essential for proper nucleosome positioning.<sup>6</sup> Despite extensive biochemical data underscoring the importance of auxiliary elements and their interactions with nucleosomal features, <sup>6,23,24</sup> the structural transitions underpinning initial remodeler recruitment and pause states remain unclear.

Here, we use single-particle cryoelectron microscopy (cryo-EM) to visualize three distinct conformations of CHD1 in complex with nucleosomes that explain the stepwise recruitment of CHD1 to its nucleosomal substrate and the rate-limiting step of remodeler pausing. We describe a previously unrecognized motif ("anchor element") conserved across all human CHD chromatin remodelers. The anchor element engages the H2A-H2B acidic patch and physically tethers the ATPase motor to the acidic patch and the DNA-binding region of CHD1. Mutations targeting the newly observed interactions impair nucleosome sliding in both CHD and ISWI remodelers, underscoring a broadly conserved mechanism.<sup>25</sup> Our findings also demonstrate how CHD1 interacts with the trimethylated tail of histone H3 in the context of a nucleosomal substrate and that H3K4me3 recognition plays only a minor role in CHD1 recruitment and nucleosome sliding in vitro.





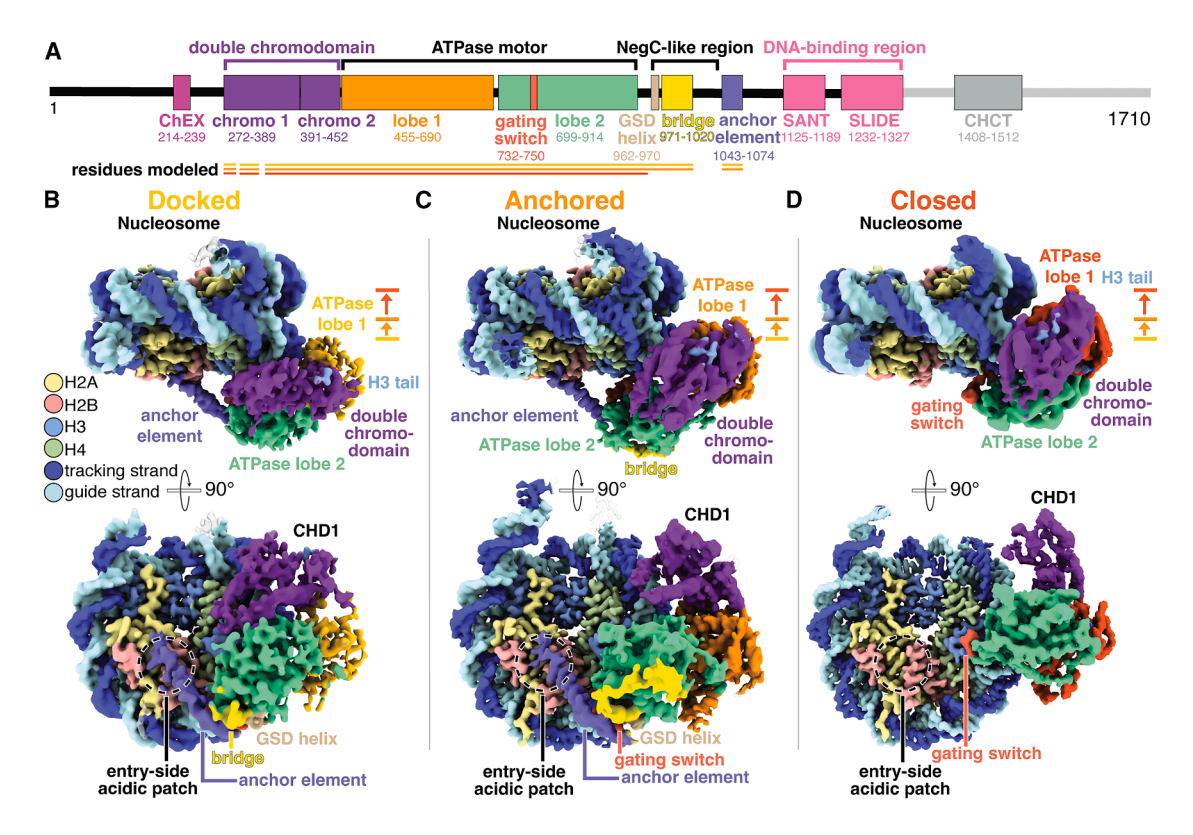


Figure 1. Structures of the CHD1-nucleosome complex in a docked, anchored, and closed state

- (A) Domain architecture of H. sapiens CHD1. Colors used throughout. Modeled residues are shown as solid lines.
- (B) Structure of the nucleosome-CHD1 complex in the docked state. The ATPase lobe 1 is shown in yellow.
- (C) Structure of the nucleosome-CHD1 complex in the anchored state. The ATPase lobe 1 is shown in orange.
- (D) Structure of the nucleosome-CHD1 complex in the closed state. The ATPase lobe 1 is shown in red.
- See also Figures S1–S5 and S7A, Tables 1 and S1, and Video S1.

### **RESULTS**

# Structural snapshots of *H. sapiens* CHD1-nucleosome complexes

To capture recruitment and regulatory states of chromatin remodeling, we formed a complex between H. sapiens CHD1 and a nucleosomal substrate. To do so, we recombinantly expressed and purified H. sapiens CHD1 (CHD1 residues 1-1,327 lacking the CHD1 helical C-terminal (CHCT) domain, referred to as CHD1 throughout) (Figures 1A and S1A; STAR Methods) and reconstituted a nucleosome on a 205 base pair (bp) DNA containing the Widom 601 nucleosome positioning sequence, 26 with 30 bps of extranucleosomal DNA flanking the Widom 601 sequence on both sides of the nucleosome (Figures S1B and S1D). Because human CHD1 recognizes H3K4me3,20 our histone H3 bears a trimethyl-lysine 4 analog of histone protein H3<sup>27</sup> (H3K4Cme3, Figure S1E). The CHD1-H3K4Cme3 nucleosome complex was formed in the presence of the transition-state analog ADP-BeF3 and purified via size exclusion chromatography (Figures S1F-S1H). The purified complex was mildly crosslinked with glutaraldehyde, and we employed single-particle cryo-EM to visualize the complex (Figures S2 and S3; STAR Methods).

Classification of the resulting dataset revealed three distinct structural conformations of CHD1 bound to the nucleosome (Figures 1B–1D and S2–S6; Video S1; Tables 1 and S1). One of these conformations corresponds to the previously characterized closed state that is commonly observed in nucleosome-bound chromatin remodeler structures<sup>22,25,28–33</sup> (Figure 1D). The other two conformations represent previously unobserved states of CHD1 (Figures 1B and 1C). Both states likely represent key intermediate stages during the remodeling process. The first state, or "docked" state, could represent initial chromatin remodeler recruitment, and the second, or "anchored" state, represents further recruitment and interspersed pausing intermediates.

### The docked state of the CHD1-nucleosome complex

The "docked state" was reconstructed from 21,168 particles with an overall resolution of 3.8 Å (Figures 1B, S3–S5, S6C, and S6D; Tables 1 and S1) and diverged significantly from previous structures of yeast and human CHD remodelers. Specifically, we observed a previously unresolved CHD1 helix, repositioning of ATPase lobe 1 and ATPase lobe 2, and repositioning of the double chromodomains. These rearrangements in the docked state likely represent an initial recruitment state of CHD1 to its nucleosome substrate.

Table 1. Cryo-EM data collection, model refinement, and validation

8
Ce
Pre
SS

	CHD1-nucleosome closed state	CHD1-nucleosome anchored state	CHD1-nucleosome docked state	Closed state with exit-side DBR	Anchored state with entry-side DBR	Docked state with entry-side DBR
Мар	map A (sharpened)/map B	map C (sharpened)/map D	map E (sharpened)/map F	map I	map H	map G
PDB ID	PDB: 9EAR	PDB: 9NH8	N/A	N/A	N/A	N/A
EMDB ID	EMD-47841	EMD-49406	EMD-47845	EMD-47857	EMD-47852	EMD-47856
Data collection and processing						
Microscope	Thermo Fisher Titan Krios	Thermo Fisher Titan Krios	Thermo Fisher Titan Krios	Thermo Fisher Titan Krios	Thermo Fisher Titan Krios	Thermo Fisher Titan Krios
Voltage (keV)	300	300	300	300	300	300
Camera	Gatan K3	Gatan K3	Gatan K3	Gatan K3	Gatan K3	Gatan K3
Magnification	105,000	105,000	105,000	105,000	105,000	105,000
Pixel size at detector (Å per pixel)	0.83	0.83	0.83	0.83	0.83	0.83
Total electron exposure $(e^- \mathring{A}^{-2})$	54.6	54.6	54.6	54.6	54.6	54.6
Exposure rate ( $e^- Å^{-2} s^{-1}$ )	17.100	17.100	17.100	17.100	17.100	17.100
Number of frames collected during exposure	50	50	50	50	50	50
Defocus range (μm)	1.0–1.8	1.0–1.8	1.0–1.8	1.0-1.8	1.0-1.8	1.0-1.8
Automation software	SerialEM	SerialEM	SerialEM	SerialEM	SerialEM	SerialEM
Energy filter slit width (eV)	20	20	20	20	20	20
Micrographs collected (no.)	24,902	24,902	24,902	24,902	24,902	24,902
Micrographs used (no.)	23,129	23,129	23,129	23,129	23,129	23,129
Total extracted particles (no.)	6,452,356	6,452,356	6,452,356	6,452,356	6,452,356	6,452,356
Refined particles (no.)	6,452,356	6,452,356	6,452,356	6,452,356	6,452,356	6,452,356
Final particles (no.)	110,418	67,512	21,168	32,699	45,520	16,853
Resolution (global, Å)						
FSC 0.5 unmasked	6.8	6.6	9.0	7.1	7.7	9.2
FSC 0.5 masked	3.5	3.6	4.5	3.8	4.0	7.1
FSC 0.143 unmasked	4.0	3.9	7.0	4.1	5.5	4.7
FSC 0.143 masked	3.1	3.2	3.8	3.3	3.5	3.9
Map sharpening B factor (Ų)	65.7	88.4	54.9	73.5	65.9	49.2
3D FSC sphericity	0.967	0.980	0.919	0.967	0.967	0.942
Map sharpening methods	cryoSPARC	cryoSPARC	cryoSPARC	cryoSPARC	cryoSPARC	cryoSPARC
Model composition						
Non-hydrogen atoms (no.)	17,990	18,518	18,176	N/A	N/A	N/A
Protein residues (no.)	1,423	1,494	1,467	N/A	N/A	N/A

(Continued on next page)

	CHD1-nucleosome closed state	CHD1-nucleosome anchored state	CHD1-nucleosome docked state	Closed state with exit-side DBR	Anchored state with entry-side DBR	Docked state with entry-side DBR
Ligands (no.)						
Nucleotide residues (no.)	316	312	306	N/A	N/A	N/A
Model refinement						
Initial models used (AlphaFold or PDB ID)	AF-O14646-F1, 3LZ0, 2B2W	AF-O14646-F1, 3LZ0, 2B2W	AF-O14646-F1, 3LZ0, 2B2W	N/A	N/A	N/A
Refinement packages	Coot, ISOLDE, PHENIX real space	Coot, ISOLDE, PHENIX real space	Coot, ISOLDE, PHENIX real space	N/A	N/A	N/A
Model-map scores						
Cross-correlation coefficient	0.77	0.77	0.68	N/A	N/A	N/A
Model resolution (Å)	3.1	3.2	3.8	N/A	N/A	N/A
FSC threshold	0.143	0.143	0.143	N/A	N/A	N/A
Mean B factors (Ų)						
Protein residues (no.)	77.03	91.10	184.51	N/A	N/A	N/A
Nucleotide residues (no.)	83.67	86.01	146.36	N/A	N/A	N/A
RMSD from ideal values						
Bond lengths (Å)	0.004	0.005	0.003	N/A	N/A	N/A
Bond angles (°)	0.653	0.963	0.499	N/A	N/A	N/A
Validation						
MolProbity score	1.16	1.60	1.59	N/A	N/A	N/A
CaBLAM outliers (%)	1.24	2.44	1.15	N/A	N/A	N/A
Clashscore	3.72	6.47	11.95	N/A	N/A	N/A
Poor rotamers (%)	0.25	0.55	0.64	N/A	N/A	N/A
C-beta deviations (%)	0.00	0.00	0.00	N/A	N/A	N/A
EMRinger score	2.63	1.74	1.27	N/A	N/A	N/A
Ramachandran plot						
Favored (%)	98.42	96.31	98.45	N/A	N/A	N/A
Allowed (%)	1.58	3.69	1.55	N/A	N/A	N/A
Outliers (%)	0.00	0.00	0.00	N/A	N/A	N/A





Here, we describe four major conformational differences between the docked state and previous structures. First, a previously unresolved but biochemically critical helix<sup>34</sup> (CHD1 residues 1043-1067) contacts ATPase lobe 2 and extends toward the entry-side H2A-H2B acidic patch, forming the anchor element (Figure 1B). Second, ATPase lobe 1 is shifted 2 bp away from the dyad compared with closed-state structures, suggesting the docked state precedes the closed state upon nucleosome binding. Third, in the docked state, ATPase lobe 2 swings away from the nucleosomal DNA, inducing an 18 Å shift compared with closed conformations (Figures 1B, S6C, and S6D). The repositioning of ATPase lobe 2 creates an open configuration between ATPase lobes 1 and 2, and we do not observe density for ADP-BeF<sub>3</sub> in the CHD1 active site (Figure S5G). This open conformation of the ATPase motor and the absence of ADP·BeF<sub>3</sub> indicate this state is not yet poised for ATP hydrolysis. Finally, the double chromodomain is shifted 12 Å toward the nucleosome's entry-side face and rotated by  ${\sim}30^{\circ}$  compared with a closed state, engages Arg 23 of the H4 tail, and forms an inhibitory interface with ATPase lobe 2<sup>6,13</sup> (Figures S5J and S6C). The inhibitory interface between the double chromodomain and ATPase lobe 2 resembles the chromodomain-ATPase lobe 2 interface observed in the crystal structure of S. cerevisiae Chd1 without a nucleosomal substrate, <sup>13</sup> suggesting that CHD1 adopts the docked conformation initially upon nucleosome binding before further engaging its nucleosomal substrates (Figure S6C).

### The anchored state of the CHD1-nucleosome complex

The "anchored state" was reconstructed from 67,512 particles with an overall resolution of 3.2 Å (Figures 1C and S3-S5; Tables 1 and S1). The anchored state shares similarities with both the docked state and the fully engaged open and closed states. Specifically, the positioning of the anchor element and ATPase lobe 2 resembles the docked state, whereas the positions of the double chromodomains and ATPase lobe 1 lie in an intermediate position between the docked and closed states (Figures 1B, 1C, and S6C). ATPase lobe 1 is shifted only 1 bp away from the dyad compared with the closed state (Figure S7A). The double chromodomain sits in a conformation similar to the closed state but is shifted 1 bp away from the dyad. Again, no density is observed for ADP·BeF<sub>3</sub> in the active site (Figure S5H). Instead, a 10 Å gap is present between ATPase lobes 1 and 2. The ATPase motor in the anchored state is not as open as in the apo Chd1 structure (12 Å gap) but exhibits a wider gap than the docked state and the S. cerevisiae Chd1-nucleosome complex without bound ATP.35 Additionally, the DNA is not distorted at superhelical location (SHL) 2, as observed for S. cerevisiae Isw1 or Chd1 in open states<sup>25,35</sup> (Figure S6D). Together, we conclude the anchored state represents an intermediate recruitment state that follows the docked state but precedes the open/closed states. The anchored state may also represent a regulatory state that the remodeler reenters during interspersed pauses in the remodeling process, as observed in single-molecule fluorescence resonance energy transfer (FRET) experiments. 4,11,12 As further discussed below, (re-)entering the anchored state allows CHD1 to sense

nucleosomal features such as the H2A-H2B acidic patch and extranucleosomal DNA to regulate remodeling outcomes.

### The closed state of the CHD1-nucleosome complex

The closed state, <sup>28</sup> derived from 110,418 particles and resolved at 3.1 Å, shows ADP·BeF<sub>3</sub> bound in the ATPase active site and largely resembles the closed states of the yeast Chd1-nucleosome complex and human CHD4-nucleosome complex<sup>28,29</sup> (Figures 1D, S2, and S5Aa; Tables 1 and S1). However, in contrast to the yeast Chd1-nucleosome complex, the DNA was not unraveled from the exit-side SHL 5 to 7.22,28 Rather, it adopted a conformation similar to the H. sapiens CHD4-nucleosome complex<sup>29</sup> (Figures S6A and S6B). We observe weak density for the DNA-binding region (residues 1,125-1,327) of CHD1 at the DNA exit site (SHL 7) and density for residue 130 of the CHD1 exit-side binding (ChEx) domain interacting with the acidic patch of the exit-side H2A-H2B dimer (Figure S5U).35 As anticipated, the CHD1 double chromodomain was found to interact with the methylated H3K4me3 residue similar to the crystal structure of the CHD1 double chromodomain in complex with H3K4me3.<sup>20</sup> In summary, the closed state resembles previously observed conformations for all chromatin remodeler families bound to a nucleosome. 25,28-33

### Mobile DNA-binding region binds entry- or exit-side DNA

Biochemical data have shown that binding of the *S. cerevisiae* Chd1 DNA-binding region to entry-side DNA directs Chd1 sliding outcomes.<sup>36</sup> However, in all published structures of nucleosome-bound Chd1, the DNA-binding region binds to exit-side extranucleosomal DNA, which has been proposed to induce a putatively inhibited state of the ATPase motor.<sup>10,28</sup> We observe the DNA-binding region on entry-side DNA in the docked and anchored states (Figures 2A, 2B, S7B, and S7C). This finding aligns with previous work indicating that the DNA-binding region senses the available extra-nucleosomal DNA at the DNA entry side and guides the repositioning of nucleosomes.<sup>6,11,37–39</sup>

Importantly, the DNA-binding region is connected to the CHD1 ATPase motor via our newly observed anchor element and the NegC-like region, suggesting a coupling between the positioning of these elements<sup>7</sup> (Figure 2D) that could explain how CHD1 senses entry-side DNA during initial nucleosome engagement and while undergoing interspersed pausing during remodeling.

In the closed state, the DNA-binding region is located above the double chromodomain and only binds the exit-side DNA at SHL 7, similarly to *S. cerevisiae* Chd1-nucleosome complex structures<sup>28</sup> (Figures 2C and S7D). Notably, the placement of the DNA-binding region correlates with the presence or absence of ADP·BeF<sub>3</sub> in the CHD1 active site, suggesting our nucleosome substrate with equal extranucleosomal DNA lengths on either side of the nucleosome and the low concentration of ADP·BeF<sub>3</sub> after gel filtration of the CHD1-nucleosome complex allowed us to capture the multiple conformations of CHD1, including the docked and anchored states. Together, these results suggest the anchored and docked states serve a regulatory role whereby CHD1 senses entry-side DNA prior to bursts of remodeling.

### **Article**



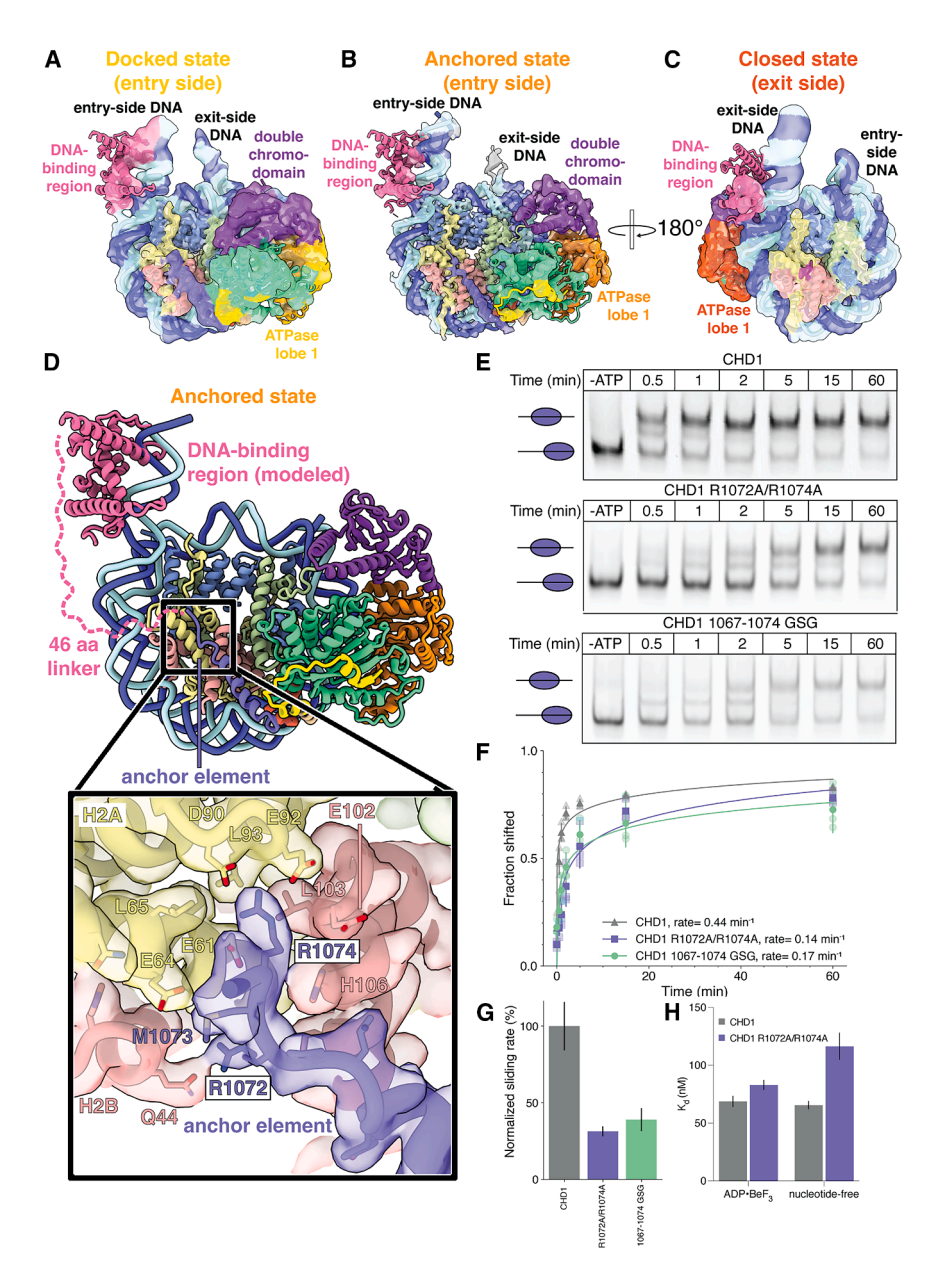


Figure 2. Interaction of the CHD1 DNA-binding region with DNA and the anchor element with the entry-side H2A-H2B dimer (A) Cryo-EM reconstruction of the docked state (map G) shows binding of the DNA-binding region (pink) to the entry-side DNA at SHL 7.

- (B) Cryo-EM reconstruction of the anchored state (map H) shows binding of the DNA-binding region (pink) to the entry-side DNA at SHL 7.
- (C) Cryo-EM reconstruction of the closed state (map I) shows binding of the DNA-binding region (pink) to the exit-side DNA at SHL 7.
- (D) The anchor element of CHD1 projects toward the acidic patch of the entry-side H2A-H2B dimer. CHD1 Arg1074 binds depression 1 of the acidic patch. Acidic patch side chains and CHD1 Arg1072 and Arg1074 are shown as sticks. Cryo-EM map (map C) is shown as a transparent surface.
- (E) CHD1 Arg1072Ala/Arg1074Ala and CHD1 1067-1074 GSG linker show a reduction in nucleosome sliding activity compared with wild-type CHD1.
- (F) Quantification of nucleosome sliding assay from (E). Experiments were conducted as triplicates. Individual data points and means with standard deviations are shown.
- (G) Nucleosome sliding rates calculated from (F). Rates were calculated based on the slope after fitting the first minute of the sliding reactions via linear regression and normalizing to the wild-type rate. Average rates with standard deviations are shown.
- (H) The CHD1 Arg1072Ala/Arg1074Ala mutant shows a 1.8-fold reduction in nucleosome-binding affinity compared with wild-type CHD1 in nucleotide-free (apo) conditions but only a minor (1.2-fold) reduction in nucleosome-binding affinity compared with wild-type CHD1 in the presence of ADP-BeF $_3$ . Nucleosome-binding affinity was determined by fluorescence polarization, and experiments were conducted as triplicates. Average dissociation constants ( $K_d$ ) with standard deviations are shown.

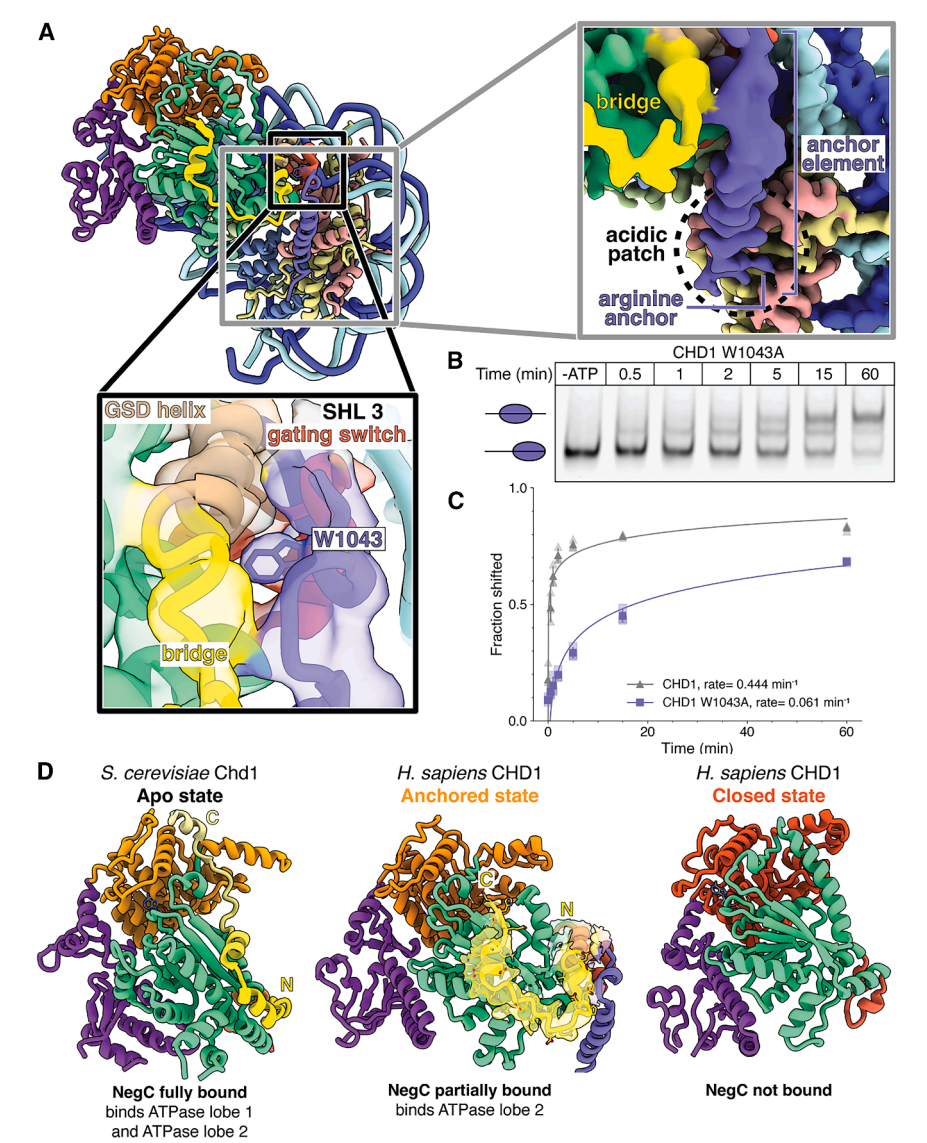
See also Figures S1A, S3, S7B–S7D, S8, and S9C, and Mendeley Data (https://data.mendeley.com/datasets/hdhcsf6k6m/1; Data S1).

# The anchor element binds the entry-side H2A-H2B acidic patch

In the docked and anchored states, we resolved an uncharacterized structural feature, the anchor element, that connects the ATPase motor with the DNA-binding region. The anchor element (CHD1 residues 1,043–1,074) is positioned next to ATPase lobe 2 and extends over the nucleosomal surface to the entry-side H2A-H2B acidic patch, where two arginine anchor residues (Arg1072 and Arg 1074) insert to physically connect ATPase lobe 2 to the acidic patch (Figure 2D). Specifically, Arg1074 inserts into depression 1 of the acidic patch as a canonical arginine anchor<sup>40</sup> and interacts with H2A residues Glu61, Asp90, Glu92, and H2B residue Glu102 (Figures 2D, S5Y, and S5Z).

Removal of the region corresponding to the anchor element leads to a robust decrease in nucleosome sliding activity not only in *S. cerevisiae* Chd1 but also in chromatin remodelers Snf2, SNF2h, 3,24 and ALC1, 14 suggesting that the interaction of the anchor element with the H2A-H2B acidic patch is broadly important for chromatin remodeling. Additionally, removal of the entry-side H2A-H2B dimer prevents nucleosome repositioning by *S. cerevisiae* Chd1, and mutation of the H2A-H2B acidic patch reduces sliding rates 2-fold. Further, the entry-side acidic patch is specifically required and confers directionality to remodeling by the ISWI chromatin remodeler. Our observation of Arg1072 and Arg1074 binding to the entry-side acidic patch rationalizes these observations, explains structurally the requirement for the entry-side H2A-H2B dimer for nucleosome





sliding by Chd1, and suggests human CHD1 is regulated similarly to ISWI. To confirm the importance of the two arginine anchor residues, we generated CHD1 mutants where the arginine anchors are mutated to alanines. Nucleosome sliding assays with the mutants revealed a 3-fold decrease in the rate of nucleosome sliding (Figures 2E–2G), indicating that the anchor element interaction with the acidic patch is a required element of remodeling by *H. sapiens* CHD1. Furthermore, mutation of residues positioned near the acidic patch (CHD1 residues 1,067–1,074) to a glycine-serine-glycine (GSG) linker does not result in a further decrease in sliding rate compared with the Arg1072Ala/Arg1074Ala mutant, highlighting the specific importance of the arginine anchors in mediating the acidic patch interaction (Figures 2E–2G).

We hypothesized that mutation of the arginine anchors decreases the affinity of CHD1 for the nucleosome in the docked and anchored states. To test this hypothesis, we used fluorescence polarization binding assays to measure the affinity of

# Figure 3. CHD1 regulatory elements cooperate to facilitate nucleosome sliding

(A) Interaction of the anchor element with ATPase lobe 2. Anchor element Trp1043 contacts the GSD helix, gating element, and the bridge. Cryo-EM reconstruction (map C) is shown as an opaque (right) or transparent (left) surface.

(B) CHD1 Trp1043Ala mutant nucleosome sliding assay.

(C) Quantification of nucleosome sliding assay from (B) shows a reduction in nucleosome sliding activity of the CHD1 Trp1043Ala mutant compared with wild-type CHD1. Experiments were conducted as triplicates. Individual data points and means with standard deviations are shown.

(D) Comparison of the interactions between the NegC-like region and the ATPase motor in the S. cerevisiae Chd1 apo state (PDB: 3MWY) and H. sapiens CHD1 anchored and closed states (this study). Cryo-EM density of the NegC-like region in the anchored state (map C) is shown as a transparent yellow surface. The S. cerevisiae Chd1 NegC-like region is comprised of residues 861–922, while the H. sapiens CHD1 NegC-like region is comprised of residues 962–1,021 (only residues 962–1,003 are visible in our model).

See also Figure S1A.

wild-type CHD1 compared with the Arg1072Ala/Arg1074Ala mutant for nucleosomes. We measured binding affinities both in the presence or absence of ADP·BeF<sub>3</sub> and on nucleosomes with or without extranucleosomal DNA. As expected, we measured similar affinities of wild-type and arginine anchor mutant CHD1 to the nucleosome with extranucleosomal DNA in the presence or absence of ADP·BeF<sub>3</sub> (Figures S9A and S9B). The similar affinities can be attributed to a strong contribution of the

DNA-binding region, the ATPase motor, and the double chromodomains. <sup>21</sup> Accordingly, the arginine anchor mutant showed similar affinities.

To eliminate the strong contribution of the DNA-binding region, we measured affinities on the nucleosomal substrate lacking extranucleosomal DNA. Loss of the DNA-binding region contribution led to a subtle reduction in binding affinities (Figures 2H and S9A–S9C). In the presence of ADP·BeF<sub>3</sub>, where the ATPase motor adopts the tightly bound closed state, we also only observed a slight reduction in binding affinity for the arginine anchor mutant compared with wild-type CHD1. However, in the reactions lacking ADP·BeF<sub>3</sub> (favoring the docked and anchored states), we observe a 1.7-fold decrease in the affinity of the Arg1072Ala/Arg1074Ala mutant compared with wild-type CHD1, indicating that the arginine anchors are important for nucleosome binding in the docked/anchored states and likely play a role in recruitment of CHD1 to nucleosomes (Figures 2H and S9C).



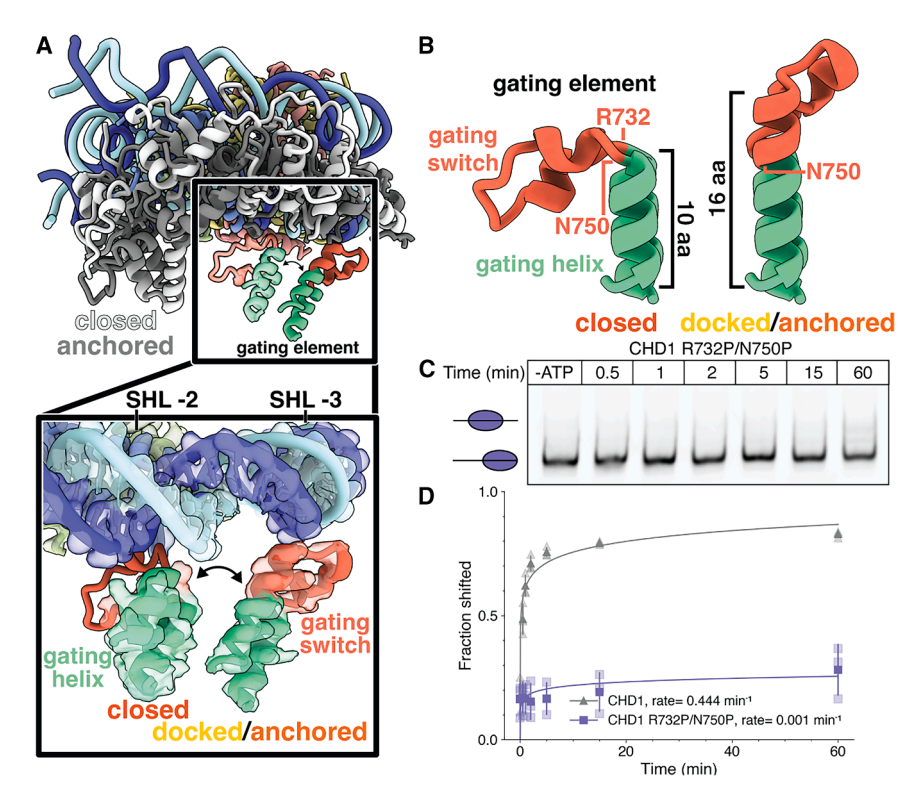


## Figure 4. Gating element conformational switch facilitates nucleosome sliding

(A) The gating element adopts different positions on the nucleosomal DNA. In the closed state, it contacts DNA at the entry-side SHL 2, whereas the anchored and docked states show the gating element interacting with DNA at SHL 3.

(B) The gating element is composed of the gating helix, gating switch, and the a-helix preceding the gating switch. The gating element adopts different conformations in the closed and anchored/docked states. The gating element undergoes a helical extension in the anchored/docked states.

(C) The CHD1 Arg732Pro/Asn750Pro mutant

shows no nucleosome sliding activity.

(D) Quantification of nucleosome sliding assay from (C). Experiments were conducted as triplicates. Individual data points and means with

See also Figure S1A.

standard deviation are shown

# The anchor element binds ATPase lobe 2, the bridge, the GSD helix, and the gating helix

The N terminus of the anchor element packs against ATPase lobe 2 in the docked and anchored states via Trp1043, suggesting it plays a role in coordinating regulatory elements to modulate sliding outcomes (Figures 1B, 1C, 3A, S5Ab, and S5Ac). Specifically, Trp1043 engages three regulatory elements of CHD1. First, Trp1043 interacts with the bridge that engages ATPase lobe 2. Second, Trp1043 contacts the "GSD helix" (CHD1 residues 962–970), which has been shown to be stimulatory for nucleosome sliding. Third, Trp1043, together with the GSD helix, sits next to a characteristic Snf2-type insertion 12 in ATPase lobe 2 called the gating helix (CHD1 residues 751–760). Like the GSD helix, the gating helix has also been shown to be indispensable for nucleosome sliding. Importantly, the equivalent residue of Trp1043 had not been visualized in yeast Chd1 and is critical for nucleosome sliding but not for ATP hydrolysis. The suggestion of the sugg

Because of the prominent placement of Trp1043 and its broad conservation across chromatin remodeler families, 30,34 we substituted this residue with alanine. Indeed, substitution of Trp1043 with alanine results in remodeling defects with a greater than 10-fold decrease in the rate of nucleosome sliding (Figures 3B and 3C). Together with our structural data, this observation suggests Trp1043 plays a critical role in coupling the bridge, GSD helix, and gating helix with H2A-H2B acidic patch binding and entry-side DNA readout via the anchor element. Because the anchor element is separated from the NegC-like region (residues 962–1,020) by only 23 residues, stable positioning of the anchor element as observed in our

anchored state structure also prevents binding of part of the NegC to ATPase lobe 1 (Figure 3D). We suggest this represents a mechanism by which CHD1 recognizes nucleosomes with an available entry-side DNA and acidic patch and repositions parts of the NegC during the

transition from an apo state into nucleosome-bound states during recruitment.

# A gating element conformational switch facilitates nucleosome sliding

The gating helix contacts Trp1043 and is critical for nucleosome sliding. The gating helix is part of a widely conserved helix-loophelix region ("gating element," CHD1 residues 720–760) located in the C-terminal portion of ATPase lobe 2. The loop of the gating helix interacts with the H3 core in our closed-state structure, consistent with interactions observed across ISWI, CHD, SWI/SNF, and INO80 chromatin remodelers. <sup>28–30,33,43–46</sup> In the docked and anchored states, the N terminus of the anchor element packs against the loop of the gating element via Trp1043, and the loop is repositioned by ~45 Å through the movement of ATPase lobe 2. This rearrangement enables the gating helix to interact with the backbone of the nucleosomal DNA at the entry-side SHL 3 (Figure 4A).

When comparing the conformation of the helix-loop-helix gating element in the closed versus the docked/anchored states, we observe a conformational change in the gating element. Like a switch, a six amino acid helical extension infiltrates the connecting gating element loop (CHD1 residues 732–750, Figure 4B). The extension of the gating helix results in the packing of the gating element against the nucleosomal DNA at SHL 3 (entry side). Notably, interaction of the gating element with SHL 3 has only been observed previously for SWR1-nucleosome complexes. 45,47 SWR1 is involved in histone replacement and is unable to slide nucleosomes. Therefore, our anchored and docked states of CHD1 demonstrate that nucleosome-sliding



competent remodelers can also undergo a conformational switch in the gating element as previously postulated but not observed and could represent an intermediate to induce a twist defect at SHL 2.48 To test whether the helical extension of the gating element itself is required for coupling nucleosome sliding to ATP hydrolysis, we mutated the two residues bordering the gating switch (Arg732 and Asn750) to prolines to disfavor helical extension in the anchored and/or docked states, though we cannot formally exclude that these mutations will also affect nucleosomal interactions in the closed state. Strikingly, we find that nucleosome sliding activity is fully abolished upon mutation of these residues, whereas ATP hydrolysis activity remains robust (Figures 4C, 4D, and S9D). In summary, our data demonstrate that the gating element undergoes a helical extension upon rearrangement from the closed to anchored/docked states that is critical for nucleosome sliding.

### The anchor and gating elements are broadly conserved

Given the biochemical evidence for the importance of the region C-terminal of the ATPase motor and the H2A-H2B acidic patch for nucleosome sliding, 8,9,14,23 we hypothesize that the mechanism of entry-side acidic patch recognition is conserved across the CHD family of chromatin remodelers. Due to sequence divergence, multiple sequence alignments, however, were unable to identify the anchor residues that mediate the interaction with the acidic patch. By examining known structures and employing AlphaFold-Multimer predictions, we predicted arginine anchor elements across the CHD, ISWI, and SWI/SNF families of chromatin remodelers (Figure S8). Specifically, we performed an AlphaFold-Multimer screen with S. cerevisiae Isw1, Isw2, Snf2, H. sapiens CHD1-9, SMARCA1 (SNF2L), SMARCA2 (BRM), and SMARCA5 (SNF2h) remodelers in the presence of an H2A-H2B dimer and potential residues that insert into the H2A-H2B acidic patch. We confirm previously observed interactions for the SWI/SNF chromatin remodeler family 9,24,49 and predict the specific arginine anchors located C-terminal of the ATPase motor for CHD1-9. These results suggest the mechanism of acidic patch recognition during remodeler recruitment and regulation is broadly conserved across chromatin remodeler families, including the ISWI<sup>50</sup> and CHD families. Accordingly, mutation of the N-terminal tryptophan of the anchor element in SMARCA5 (Trp730Ala) or disruption of the gating switch in SMARCA5 results in a significant reduction in nucleosome sliding activity (Figures S9E-S9G). Together, these results implicate that during recruitment, ISWI and CHD remodelers adopt conformations like our anchored and docked CHD1 states.

# CHD1 auto-inhibition and H3K4Cme3 binding by the double chromodomain

We observe notable changes in the autoregulatory double chromodomain between our three states and visualize the recognition of H3K4Cme3 by nucleosome-bound CHD1 (Figures 5A and 5B). In all three states, the double chromodomain binds the H3K4Cme3 residue via its aromatic cage formed by residues Trp322 and Trp325 (Figure 5B). The region between the trimethylated tail and H3 residue 39 remains unresolved. We tested if trimethylation of H3K4 influences affinity to the nucleosomal

substrate or nucleosome sliding rates. We did not observe a change in sliding rate (Figure 5C). Fluorescence polarization affinity measurements revealed a slight increase in affinity for the H3K4Cme3 nucleosome compared with a canonical nucleosome (Figure 5D). Contrary to initial expectations, our data indicate that H3K4me3 only plays a minor role in directing CHD1 binding to relevant methylated nucleosomes *in vitro*.

The H3K4me3-bound double chromodomain undergoes significant conformational changes across different states. In the docked state, it adopts an auto-inhibitory conformation that is subsequently relieved in the anchored state and remains relieved through the open and closed states. In the docked state, the double chromodomain rotates toward the nucleosomal face, where Glu369 and Glu372 bind H4 tail Arg23, preventing ATPase closure (Figure 5A). The transition to the anchored state involves a rotation away from the entry-side nucleosome face, where the chromodomain engages H4 tail Arg17 and contacts SHL 1 DNA, enabling ATPase closure (Figure 5A). In the closed state, the chromodomains rotate further, allowing ATPase lobe 2 to engage H4 tail Arg17 as the ATPase motor closes (Figure 5A).

Previous studies with *S. cerevisiae* Chd1 showed that mutations at the chromodomain-ATPase lobe 2 interface enhance nucleosome sliding and ATP hydrolysis while reducing dependency on entry-side DNA and the H4 tail. Our structural data confirm the double chromodomain's regulatory role. Surprisingly, we find that the double chromodomain still stabilizes an ATP hydrolysis-incompetent conformation in the docked state even when partially engaged with the nucleosome. Together with the changing H4 tail interactions, our structures explain how auto-inhibition by the double chromodomain is relieved upon nucleosome binding.<sup>7,51</sup>

### **DISCUSSION**

Our biochemical and structural observations provide an expanded model for the regulation of nucleosome sliding. We provide structural evidence that CHD1 and other remodelers that slide nucleosomes not only adopt open and closed states but also additional conformations during recruitment and pausing (Figure 5E). Specifically, we have identified two previously uncharacterized conformations of the CHD1 remodeler bound to a nucleosome that provide a rationale for stepwise recruitment and autoregulation of CHD1 through recognition of the entry-side DNA and the H2A-H2B dimer, resulting in rearrangements of essential elements including the NegC-like region with the bridge and GSD helix, the gating element, and the double chromodomain of CHD1. A low-resolution conformation resembling our anchored/docked states has also been observed for the ALC1 remodeler, indicating other remodelers may adopt similar states. 52 The docked and anchored states of CHD1 highlight an unappreciated mode of CHD family remodeler regulation that is dependent on acidic patch binding. This concept extends to other chromatin remodelers that rely on acidic patch interactions, such as ISWI, SWI/SNF, and INO80 complexes, which may also undergo conformational transitions depending on competition with other acidic patch-binding proteins. 53-55 The presence of histone chaperones, chromatin-bound factors, or even



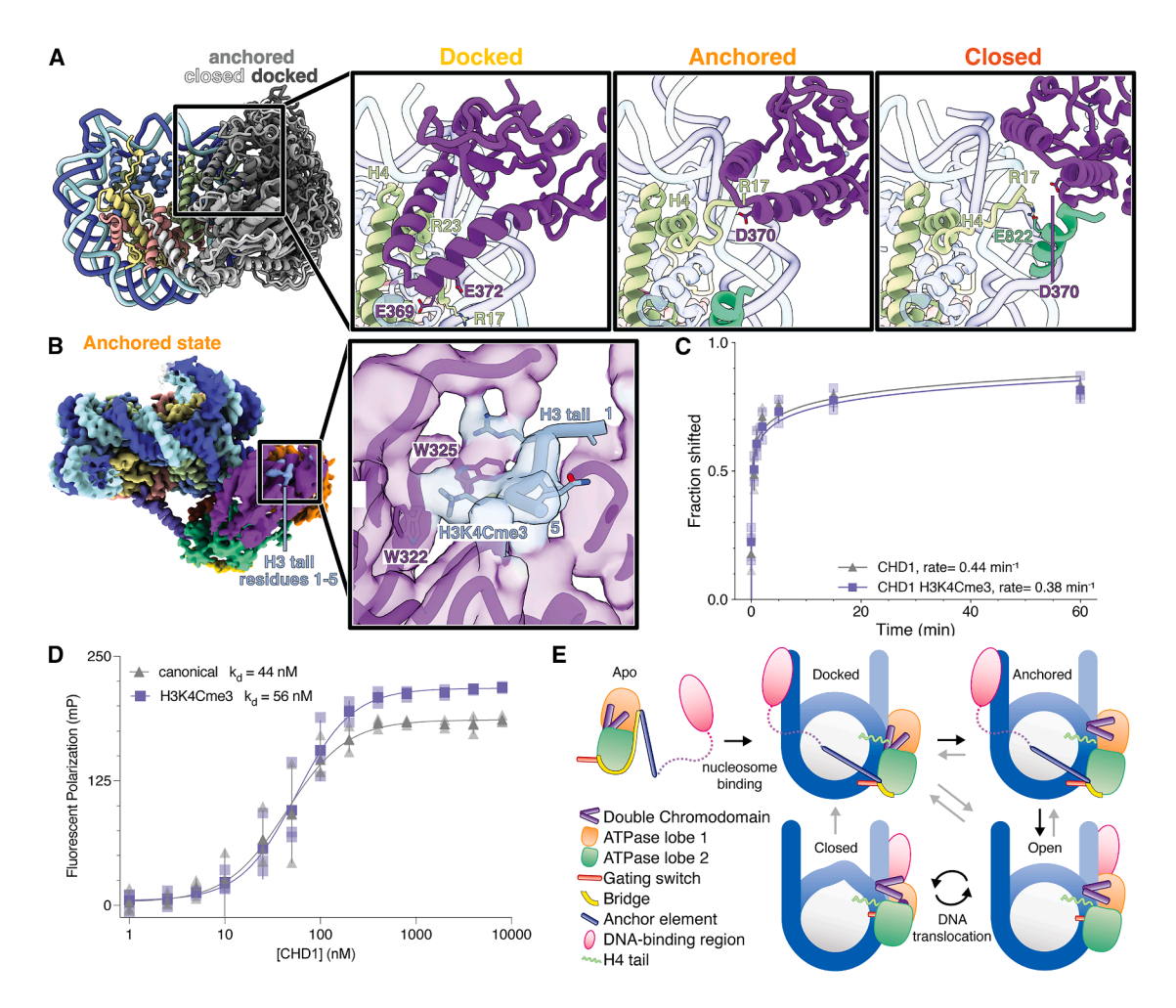


Figure 5. H3 and H4 tail interaction of the CHD1 double chromodomain

(A) The double chromodomain undergoes significant conformational rearrangements between the docked, anchored, and closed states and directly interacts with the H4 N-terminal tail. The double chromodomain engages Arg23 of the H4 tail in the docked state and engages Arg17 in the anchored state. In the closed state, ATPase lobe 2 engages Arg17 of the H4 tail.

(B) Interaction of CHD1 with the H3K4Cme3 residue of histone protein H3 in the anchored state. The H3K4Cme3 residue inserts into the aromatic pocket formed by the double chromodomain residues CHD1 Trp322 and CHD1 Trp325. H3K4Cme3, CHD1 Trp322, and CHD1 Trp325 atoms are shown as sticks with the cryo-EM density overlayed as a transparent surface (map C).

(C) Trimethylation of the H3 tail at K4 does not affect the rate of nucleosome sliding by CHD1. Experiments were conducted as biological triplicates. Individual data points and means with standard deviations are shown.

(D) Trimethylation of the H3 tail at K4 does not affect the dissociation constant of binding by CHD1. Experiments were conducted as triplicates. Individual data points and means with standard deviations are shown.

(E) Model illustrating steps during the process of chromatin remodeling, including previously uncharacterized conformations presented in this study. See also Figure S1E and Mendeley Data (https://data.mendeley.com/datasets/hdhcsf6k6m/1; Data S1).

transient modifications of histones may therefore directly regulate the efficiency and specificity of nucleosome remodeling by controlling the availability of the acidic patch. Going forward, the anchored and docked states may also represent novel states for therapeutic discovery. Furthermore, the minor effects of H3K4me3 presence on CHD1 recruitment and activity clarify that CHD1 recruitment to actively transcribed regions likely requires additional factors and/or histone modifications. Indeed, the transcription elongation factor RTF1 binds CHD1 to direct it to transcription elongation complexes. <sup>56</sup>

Our data suggest a multi-step mechanism for CHD1 action. Upon binding of CHD1 to the nucleosome, interaction

of the DNA-binding region with entry-side DNA positions the anchor helix on the entry-side H2A-H2B dimer, and CHD1 transitions from the unbound apo state into the catalytically inactive docked state. The double chromodomain binds Arg23 of the H4 tail and occludes closure of the ATPase lobe 2, the NegC-like region partially binds ATPase lobe 2, and the gating element adopts an extended conformation akin to the Swr1 gating element, <sup>45,47</sup> engaging nucleosomal DNA at SHL 3 of the entry-side DNA gyre. Then, upward swinging of the double chromodomain to engage Arg17 of the H4 tail and SHL1 DNA relieves the steric block of ATPase lobe 2, and ATPase lobe 1 moves one nucleotide along the nucleosomal



DNA. This places CHD1 into the anchored conformation, an intermediate state that senses entry-side DNA. Depending on extranucleosomal DNA availability, CHD1 may flip sides of the nucleosome while remaining tethered to DNA to direct nucleosome sliding outcomes, similar to the mechanism of directed histone exchange by Swr1 complexes.<sup>57</sup> Once in the anchored state, CHD1 can transition to the open state, 35 creating a tracking strand bulge, disengaging the anchor element, binding exit-side DNA, and collapsing the extended gating switch. Finally, ATP binding leads to closure of the ATPase, ATP hydrolysis, and translocation of nucleosomal DNA via a twist defect/diffusion-based mechanism. 48 As observed by singlemolecule experiments, 4,11,12 CHD1 occasionally re-enters the anchored/docked states and pauses to sense entry-side DNA, preventing DNA from being pulled in past the nucleosome entry point.

Together, our results visualize a direct coupling of the H2A-H2B acidic patch with the ATPase motor of CHD family remodelers, providing a geometric rationale for the sensing of entry-side DNA. Our data agree with (1) existing models that proposed binding of the DNA-binding region on the entry-side DNA to establish efficient coupling of ATP hydrolysis and nucleosome sliding<sup>1,8,10,58,59</sup> and (2) with observations of interspersed pauses between multi-base pair bursts of translocation where the remodeler may enter the anchored and docked conformations. 4,11,12 Because the transition into DNA translocation-competent states from the docked and anchored states is likely rate-limiting, the chromatin remodeling reaction will ultimately be rate sensitive to DNA sensing.<sup>60</sup> Importantly, structural and functional conservation of the anchor, gating, and NegC-like elements suggests our model is broadly applicable to chromatin remodeling enzymes, supporting an expanded but shared model of chromatin remodeling that clarifies remodeler recruitment and interspersed pausing during remodeling.<sup>25</sup>

### **Limitations of the study**

The heterogeneity of the sample and flexibility of the CHD1-nucleosome complex only allowed detailed cryo-EM reconstructions by employing masked classifications and combining multiple maps to interpret our data. In our cryo-EM map of the docked state, the ATPase lobe 2 is mobile. Therefore, we were only able to assign and build the secondary structure of the ATPase lobe 2 for the docked state. We visualize the mobile DNA-binding region of CHD1 at low resolution but are unable to build a high-confidence pseudo-atomic model for the DNA-binding region in any of our states.

Our structural data reveal positional shifts of ATPase lobe 1 relative to the nucleosome dyad: a 1-bp displacement in the anchored state and a 2-bp displacement in the docked state compared with the closed state. This stepwise repositioning, combined with the inhibitory conformation of the double chromodomain observed specifically in the docked state, strongly suggests a sequential progression from docked to anchored to closed states during the CHD1 remodeling cycle. Nevertheless, we acknowledge several limitations to this model: (1) we cannot definitively exclude alternative state transitions or additional conformational intermediates during the remodeling process,

particularly during pausing events, and (2) while our *in vitro* biochemical assays indicate that H3K4Cme3 has minimal effect on CHD1 binding and sliding activity under reconstituted conditions, this modification might exert more significant regulatory influence in the complex chromatin environment *in vivo*, potentially through interactions with additional factors absent in our purified system.

#### **RESOURCE AVAILABILITY**

#### **Lead contact**

Correspondence and requests should be addressed to the lead contact, Lucas Farnung (lucas\_farnung@hms.harvard.edu).

#### Materials availability

Materials are available from Lucas Farnung upon request and a completed materials transfer agreement with Harvard University.

#### Data and code availability

- Cryo-EM reconstructions have been deposited at the Electron Microscopy Data Bank (EMDB) as accession codes EMDB: EMD-47841, EMDB: EMD-47857, EMDB: EMD-49406, EMDB: EMD-47852, EMDB: EMD-47845, and EMDB: EMD-47856 and are publicly available as of the date of publication. Structural coordinates for the CHD1-nucleosome anchored state and CHD1-nucleosome closed state have been deposited at the Research Collaboratory for Structural Bioinformatics Protein Data Bank (RCSB PDB) as PDB: 9EAR and PDB: 9NH8 and are publicly available as of the date of publication. The raw fluorescence polarization data and uncropped gel images produced during this study have been deposited into the Mendeley database as accession code <a href="https://doi.org/10.17632/hdhcsf6k6m.1">https://doi.org/10.17632/hdhcsf6k6m.1</a> and are publicly available as of the date of publication.
- This paper does not report original code.
- Any additional information required to reanalyze the data reported in this
  paper is available from the lead contact upon request.

### **ACKNOWLEDGMENTS**

We thank all members of the Farnung lab for discussions. We thank Felix Stein-ruecke and Manuel Osorio Valeriano for support with insect cell maintenance. We thank Maik Engeholm for discussions. We thank Seychelle M. Vos for discussions, advice, and critical reading of the manuscript. This research is supported by the NIH Director's New Innovator Award (DP2-ES036404) and a Harvard Medical School Q-FASTR pilot grant to L.F.

### **AUTHOR CONTRIBUTIONS**

L.F. and A.M.J. cloned protein expression constructs. A.M.J. expressed and purified all protein components, conducted biochemical experiments, prepared the complexes for cryo-EM, and collected cryo-EM data. A.M.J. processed all cryo-EM data and built models with the help of L.F. L.F. designed and supervised research. A.M.J. and L.F. wrote the manuscript.

### **DECLARATION OF INTERESTS**

The authors declare no competing interests.

### DECLARATION OF GENERATIVE AI AND AI-ASSISTED TECHNOLOGIES IN THE WRITING PROCESS

During the preparation of this work, the authors used ChatGPT in order to revise the text for clarity and conciseness. After using this tool/service, the authors reviewed and edited the content as needed and take full responsibility for the content of the publication.

### **Article**



#### **STAR**\*METHODS

Detailed methods are provided in the online version of this paper and include the following:

- KEY RESOURCES TABLE
- EXPERIMENTAL MODEL AND STUDY PARTICIPANT DETAILS
  - Cell culture
- METHOD DETAILS
  - O Cloning & mutagenesis
  - Protein expression
  - Protein purification
  - o Octamer formation and nucleosome reconstitution
  - Nucleosome sliding assay
  - O NADH-coupled ATP hydrolysis assay
  - o Fluorescence polarization affinity measurement assay
  - Complex formation for cryo-EM
  - Sample preparation for cryo-EM
  - o Cryo-EM data collection & analysis
  - o Model building & refinement
  - o AlphaFold2 screen
  - o Figure generation
- QUANTIFICATION AND STATISTICAL ANALYSIS
- ADDITIONAL RESOURCES

#### SUPPLEMENTAL INFORMATION

Supplemental information can be found online at https://doi.org/10.1016/j.molcel.2025.04.020.

Received: November 14, 2024 Revised: February 26, 2025 Accepted: April 16, 2025 Published: May 6, 2025

### REFERENCES

- Clapier, C.R., Iwasa, J., Cairns, B.R., and Peterson, C.L. (2017). Mechanisms of action and regulation of ATP-dependent chromatin-re-modelling complexes. Nat. Rev. Mol. Cell Biol. 18, 407–422. https://doi.org/10.1038/nrm.2017.26.
- Clapier, C.R., and Cairns, B.R. (2009). The Biology of Chromatin Remodeling Complexes. Annu. Rev. Biochem. 78, 273–304. https://doi. org/10.1146/annurev.biochem.77.062706.153223.
- Li, M., Xia, X., Tian, Y., Jia, Q., Liu, X., Lu, Y., Li, M., Li, X., and Chen, Z. (2019). Mechanism of DNA translocation underlying chromatin remodelling by Snf2. Nature 567, 409–413. https://doi.org/10.1038/s41586-019-1029-2
- Sabantsev, A., Levendosky, R.F., Zhuang, X., Bowman, G.D., and Deindl, S. (2019). Direct observation of coordinated DNA movements on the nucleosome during chromatin remodelling. Nat. Commun. 10, 1720. https://doi.org/10.1038/s41467-019-09657-1.
- Winger, J., Nodelman, I.M., Levendosky, R.F., and Bowman, G.D. (2018).
   A twist defect mechanism for ATP-dependent translocation of nucleosomal DNA. Elife 7, e34100. https://doi.org/10.7554/eLife.34100.
- Nodelman, I.M., Shen, Z., Levendosky, R.F., and Bowman, G.D. (2021). Autoinhibitory elements of the Chd1 remodeler block initiation of twist defects by destabilizing the ATPase motor on the nucleosome. Proc. Natl. Acad. Sci. USA 118, e2014498118. https://doi.org/10.1073/pnas. 2014498118
- Clapier, C.R., and Cairns, B.R. (2012). Regulation of ISWI involves inhibitory modules antagonized by nucleosomal epitopes. Nature 492, 280–284. https://doi.org/10.1038/nature11625.
- Gamarra, N., Johnson, S.L., Trnka, M.J., Burlingame, A.L., and Narlikar, G.
   J. (2018). The nucleosomal acidic patch relieves auto-inhibition by

- the ISWI remodeler SNF2h. eLife 7, e35322. https://doi.org/10.7554/eLife.35322.
- Sen, P., Vivas, P., Dechassa, M.L., Mooney, A.M., Poirier, M.G., and Bartholomew, B. (2013). The SnAC Domain of SWI/SNF Is a Histone Anchor Required for Remodeling. Mol. Cell. Biol. 33, 360–370. https://doi.org/10.1128/mcb.00922-12.
- Nodelman, I.M., Bleichert, F., Patel, A., Ren, R., Horvath, K.C., Berger, J. M., and Bowman, G.D. (2017). Interdomain Communication of the Chd1 Chromatin Remodeler across the DNA Gyres of the Nucleosome. Mol. Cell 65, 447–459.e6. https://doi.org/10.1016/j.molcel.2016.12.011.
- Zhong, Y., Moghaddas Sani, H.M., Paudel, B.P., Low, J.K.K., Silva, A.P. G., Mueller, S., Deshpande, C., Panjikar, S., Reid, X.J., Bedward, M.J., et al. (2022). The role of auxiliary domains in modulating CHD4 activity suggests mechanistic commonality between enzyme families. Nat. Commun. 13, 7524. https://doi.org/10.1038/s41467-022-35002-0.
- Blosser, T.R., Yang, J.G., Stone, M.D., Narlikar, G.J., and Zhuang, X. (2009). Dynamics of nucleosome remodelling by individual ACF complexes. Nature 462, 1022–1027. https://doi.org/10.1038/nature08627.
- Hauk, G., McKnight, J.N., Nodelman, I.M., and Bowman, G.D. (2010). The Chromodomains of the Chd1 Chromatin Remodeler Regulate DNA Access to the ATPase Motor. Mol. Cell 39, 711–723. https://doi.org/10.1016/j.molcel.2010.08.012.
- Lehmann, L.C., Bacic, L., Hewitt, G., Brackmann, K., Sabantsev, A., Gaullier, G., Pytharopoulou, S., Degliesposti, G., Okkenhaug, H., Tan, S., et al. (2020). Mechanistic Insights into Regulation of the ALC1 Remodeler by the Nucleosome Acidic Patch. Cell Rep. 33, 108529. https://doi.org/10.1016/j.celrep.2020.108529.
- Simic, R., Lindstrom, D.L., Tran, H.G., Roinick, K.L., Costa, P.J., Johnson, A.D., Hartzog, G.A., and Arndt, K.M. (2003). Chromatin remodeling protein Chd1 interacts with transcription elongation factors and localizes to transcribed genes. Embo J. 22, 1846–1856. https://doi.org/10.1093/emboj/cdg179.
- Skene, P.J., Hernandez, A.E., Groudine, M., and Henikoff, S. (2014). The nucleosomal barrier to promoter escape by RNA polymerase II is overcome by the chromatin remodeler Chd1. Elife 3, e02042. https://doi.org/ 10.7554/eLife.02042.
- Zhou, J., Li, J., Serafim, R.B., Ketchum, S., Ferreira, C.G., Liu, J.C., Coe, K. A., Price, B.D., and Yusufzai, T. (2018). Human CHD1 is required for early DNA-damage signaling and is uniquely regulated by its N terminus. Nucleic Acids Res. 46, 3891–3905. https://doi.org/10.1093/nar/gky128.
- Kari, V., Mansour, W.Y., Raul, S.K., Baumgart, S.J., Mund, A., Grade, M., Sirma, H., Simon, R., Will, H., Dobbelstein, M., et al. (2016). Loss of CHD1 causes DNA repair defects and enhances prostate cancer therapeutic responsiveness. EMBO Rep. 17, 1609–1623. https://doi.org/10.15252/ embr.201642352.
- Burkhardt, L., Fuchs, S., Krohn, A., Masser, S., Mader, M., Kluth, M., Bachmann, F., Huland, H., Steuber, T., Graefen, M., et al. (2013). CHD1 Is a 5q21 Tumor Suppressor Required for ERG Rearrangement in Prostate Cancer. Cancer Res. 73, 2795–2805. https://doi.org/10.1158/ 0008-5472.can-12-1342.
- Sims, R.J., Chen, C.-F., Santos-Rosa, H., Kouzarides, T., Patel, S.S., and Reinberg, D. (2005). Human but Not Yeast CHD1 Binds Directly and Selectively to Histone H3 Methylated at Lysine 4 via Its Tandem Chromodomains. J. Biol. Chem. 280, 41789–41792. https://doi.org/10. 1074/jbc.c500395200.
- Nodelman, I.M., and Bowman, G.D. (2013). Nucleosome sliding by Chd1 does not require rigid coupling between DNA-binding and ATPase domains. EMBO Rep. 14, 1098–1103. https://doi.org/10.1038/embor. 2013.158.
- Sundaramoorthy, R., Hughes, A.L., El-Mkami, H., Norman, D.G., Ferreira, H., and Owen-Hughes, T. (2018). Structure of the chromatin remodelling enzyme Chd1 bound to a ubiquitinylated nucleosome. Elife 7, e35720. https://doi.org/10.7554/eLife.35720.



- Levendosky, R.F., Sabantsev, A., Deindl, S., and Bowman, G.D. (2016).
   The Chd1 chromatin remodeler shifts hexasomes unidirectionally. eLife 5, e21356. https://doi.org/10.7554/eLife.21356.
- Dao, H.T., Dul, B.E., Dann, G.P., Liszczak, G.P., and Muir, T.W. (2020). A basic motif anchoring ISWI to nucleosome acidic patch regulates nucleosome spacing. Nat. Chem. Biol. 16, 134–142. https://doi.org/10.1038/ s41589-019-0413-4
- Yan, L., Wu, H., Li, X., Gao, N., and Chen, Z. (2019). Structures of the ISWInucleosome complex reveal a conserved mechanism of chromatin remodeling. Nat. Struct. Mol. Biol. 26, 258–266. https://doi.org/10.1038/s41594-019-0199-9.
- Lowary, P.T., and Widom, J. (1998). New DNA sequence rules for high affinity binding to histone octamer and sequence-directed nucleosome positioning11Edited. J. Mol. Biol. 276, 19–42. https://doi.org/10.1006/jmbi.1997.1494.
- Simon, M.D., and Shokat, K.M. (2012). A Method to Site-Specifically Incorporate Methyl-Lysine Analogues into Recombinant Proteins. Methods Enzymol. 512, 57–69. https://doi.org/10.1016/b978-0-12-391940-3.00003-2
- Farnung, L., Vos, S.M., Wigge, C., and Cramer, P. (2017). Nucleosome– Chd1 structure and implications for chromatin remodelling. Nature 550, 539–542. https://doi.org/10.1038/nature24046.
- Farnung, L., Ochmann, M., and Cramer, P. (2020). Nucleosome-CHD4 chromatin remodeler structure maps human disease mutations. eLife 9, e56178. https://doi.org/10.7554/eLife.56178.
- Armache, J.P., Gamarra, N., Johnson, S.L., Leonard, J.D., Wu, S., Narlikar, G.J., and Cheng, Y. (2019). Cryo-EM structures of remodelernucleosome intermediates suggest allosteric control through the nucleosome. eLife 8, e46057. https://doi.org/10.7554/eLife.46057.
- Zhang, M., Jungblut, A., Kunert, F., Hauptmann, L., Hoffmann, T., Kolesnikova, O., Metzner, F., Moldt, M., Weis, F., DiMaio, F., et al. (2023). Hexasome-INO80 complex reveals structural basis of noncanonical nucleosome remodeling. Science 381, 313–319. https://doi.org/10. 1126/science.adf6287.
- He, S., Wu, Z., Tian, Y., Yu, Z., Yu, J., Wang, X., Li, J., Liu, B., and Xu, Y. (2020). Structure of nucleosome-bound human BAF complex. Science 367, 875–881. https://doi.org/10.1126/science.aaz9761.
- Liu, X., Li, M., Xia, X., Li, X., and Chen, Z. (2017). Mechanism of chromatin remodelling revealed by the Snf2-nucleosome structure. Nature 544, 440–445. https://doi.org/10.1038/nature22036.
- Patel, A., McKnight, J.N., Genzor, P., and Bowman, G.D. (2011).
   Identification of Residues in Chromodomain Helicase DNA-Binding Protein 1 (Chd1) Required for Coupling ATP Hydrolysis to Nucleosome Sliding. J. Biol. Chem. 286, 43984–43993. https://doi.org/10.1074/jbc. M111.282970.
- Nodelman, I.M., Das, S., Faustino, A.M., Fried, S.D., Bowman, G.D., and Armache, J.-P. (2022). Nucleosome recognition and DNA distortion by the Chd1 remodeler in a nucleotide-free state. Nat. Struct. Mol. Biol. 29, 121–129. https://doi.org/10.1038/s41594-021-00719-x.
- McKnight, J.N., Jenkins, K.R., Nodelman, I.M., Escobar, T., and Bowman, G.D. (2011). Extranucleosomal DNA Binding Directs Nucleosome Sliding by Chd1. Mol. Cell. Biol. 31, 4746–4759. https://doi.org/10.1128/mcb. 05735-11.
- Stockdale, C., Flaus, A., Ferreira, H., and Owen-Hughes, T. (2006).
   Analysis of Nucleosome Repositioning by Yeast ISWI and Chd1 Chromatin Remodeling Complexes. J. Biol. Chem. 281, 16279–16288. https://doi.org/10.1074/jbc.m600682200.
- Yang, J.G., Madrid, T.S., Sevastopoulos, E., and Narlikar, G.J. (2006). The chromatin-remodeling enzyme ACF is an ATP-dependent DNA length sensor that regulates nucleosome spacing. Nat. Struct. Mol. Biol. 13, 1078–1083. https://doi.org/10.1038/nsmb1170.
- Kassabov, S.R., Henry, N.M., Zofall, M., Tsukiyama, T., and Bartholomew,
   B. (2002). High-Resolution Mapping of Changes in Histone-DNA Contacts

- of Nucleosomes Remodeled by ISW2. Mol. Cell. Biol. 22, 7524–7534. https://doi.org/10.1128/mcb.22.21.7524-7534.2002.
- McGinty, R.K., and Tan, S. (2021). Principles of nucleosome recognition by chromatin factors and enzymes. Curr. Opin. Struct. Biol. 71, 16–26. https://doi.org/10.1016/j.sbi.2021.05.006.
- Levendosky, R.F., and Bowman, G.D. (2019). Asymmetry between the two acidic patches dictates the direction of nucleosome sliding by the ISWI chromatin remodeler. eLife 8, e45472. https://doi.org/10.7554/ eLife.45472.
- Dürr, H., Körner, C., Müller, M., Hickmann, V., and Hopfner, K.-P. (2005).
   X-Ray Structures of the Sulfolobus solfataricus SWI2/SNF2 ATPase
   Core and Its Complex with DNA. Cell 121, 363–373. https://doi.org/10.1016/j.cell.2005.03.026.
- Dann, G.P., Liszczak, G.P., Bagert, J.D., Müller, M.M., Nguyen, U.T.T., Wojcik, F., Brown, Z.Z., Bos, J., Panchenko, T., Pihl, R., et al. (2017). ISWI chromatin remodellers sense nucleosome modifications to determine substrate preference. Nature 548, 607–611. https://doi.org/10.1038/nature23671.
- 44. Sundaramoorthy, R., Hughes, A.L., Singh, V., Wiechens, N., Ryan, D.P., El-Mkami, H., Petoukhov, M., Svergun, D.I., Treutlein, B., Quack, S., et al. (2017). Structural reorganization of the chromatin remodeling enzyme Chd1 upon engagement with nucleosomes. Elife 6, e22510. https://doi.org/10.7554/eLife.22510.
- Willhoft, O., Ghoneim, M., Lin, C.-L., Chua, E.Y.D., Wilkinson, M., Chaban, Y., Ayala, R., McCormack, E.A., Ocloo, L., Rueda, D.S., et al. (2018). Structure and dynamics of the yeast SWR1-nucleosome complex. Science 362, eaat7716. https://doi.org/10.1126/science.aat7716.
- Eustermann, S., Schall, K., Kostrewa, D., Lakomek, K., Strauss, M., Moldt, M., and Hopfner, K.-P. (2018). Structural basis for ATP-dependent chromatin remodelling by the INO80 complex. Nature 556, 386–390. https://doi.org/10.1038/s41586-018-0029-y.
- Louder, R.K., Park, G., Ye, Z., Cha, J.S., Gardner, A.M., Lei, Q., Ranjan, A., Höllmüller, E., Stengel, F., Pugh, B.F., et al. (2024). Molecular basis of global promoter sensing and nucleosome capture by the SWR1 chromatin remodeler. Cell 187, 6849–6864.e18. https://doi.org/10.1016/j.cell.2024. 09.007.
- Nodelman, I.M., and Bowman, G.D. (2021). Biophysics of Chromatin Remodeling. Annu. Rev. Biophys. 50, 73–93. https://doi.org/10.1146/annurev-biophys-082520-080201.
- Sen, P., Ghosh, S., Pugh, B.F., and Bartholomew, B. (2011). A new, highly conserved domain in Swi2/Snf2 is required for SWI/SNF remodeling. Nucleic Acids Res. 39, 9155–9166. https://doi.org/10.1093/nar/gkr622.
- Li, L., Chen, K., Sia, Y., Hu, P., Ye, Y., and Chen, Z. (2024). Structure of the ISW1a complex bound to the dinucleosome. Nat. Struct. Mol. Biol. 31, 266–274. https://doi.org/10.1038/s41594-023-01174-6.
- Ferreira, H., Flaus, A., and Owen-Hughes, T. (2007). Histone Modifications Influence the Action of Snf2 Family Remodelling Enzymes by Different Mechanisms. J. Mol. Biol. 374, 563–579. https://doi.org/10.1016/j.jmb. 2007.09.059.
- Bacic, L., Gaullier, G., Sabantsev, A., Lehmann, L.C., Brackmann, K., Dimakou, D., Halic, M., Hewitt, G., Boulton, S.J., and Deindl, S. (2021).
   Structure and dynamics of the chromatin remodeler ALC1 bound to a PARylated nucleosome. eLife 10, e71420. https://doi.org/10.7554/eLife.71420.
- Skrajna, A., Goldfarb, D., Kedziora, K.M., Cousins, E.M., Grant, G.D., Spangler, C.J., Barbour, E.H., Yan, X., Hathaway, N.A., Brown, N.G., et al. (2020). Comprehensive nucleosome interactome screen establishes fundamental principles of nucleosome binding. Nucleic Acids Res. 48, 9415–9432. https://doi.org/10.1093/nar/qkaa544.
- Liu, Z., Wu, Y., Mao, X., Kwan, K.C.J., Cheng, X., Li, X., Jing, Y., and Li, X. D. (2023). Development of multifunctional synthetic nucleosomes to interrogate chromatin-mediated protein interactions. Sci. Adv. 9, eade5186. https://doi.org/10.1126/sciadv.ade5186.

### **Article**



- James, A.M., Schmid, E.W., Walter, J.C., and Farnung, L. (2024). In silico screening identifies SHPRH as a novel nucleosome acidic patch interactor. Preprint at bioRxiv. https://doi.org/10.1101/2024.06.26.600687.
- Tripplehorn, S.A., Shirra, M.K., Lardo, S.M., Marvil, H.G., Hainer, S.J., and Arndt, K.M. (2024). A direct interaction between the Chd1 CHCT domain and Rtf1 controls Chd1 distribution and nucleosome positioning on active genes. Preprint at bioRxiv. https://doi.org/10.1101/2024.12.06.627179.
- Girvan, P., Jalal, A.S.B., McCormack, E.A., Skehan, M.T., Knight, C.L., Wigley, D.B., and Rueda, D.S. (2024). Nucleosome flipping drives kinetic proofreading and processivity by SWR1. Nature 636, 251–257. https:// doi.org/10.1038/s41586-024-08152-y.
- Ryan, D.P., and Owen-Hughes, T. (2011). Snf2-family proteins: chromatin remodellers for any occasion. Curr. Opin. Chem. Biol. 15, 649–656. https:// doi.org/10.1016/j.cbpa.2011.07.022.
- Narlikar, G.J., Sundaramoorthy, R., and Owen-Hughes, T. (2013).
   Mechanisms and Functions of ATP-Dependent Chromatin-Remodeling Enzymes. Cell 154, 490–503. https://doi.org/10.1016/j.cell.2013.07.011.
- Leonard, J.D., and Narlikar, G.J. (2015). A Nucleotide-Driven Switch Regulates Flanking DNA Length Sensing by a Dimeric Chromatin Remodeler. Mol. Cell 57, 850–859. https://doi.org/10.1016/j.molcel. 2015.01.008.
- Gradia, S.D., Ishida, J.P., Tsai, M.-S., Jeans, C., Tainer, J.A., and Fuss, J. O. (2017). MacroBac: New Technologies for Robust and Efficient Large-Scale Production of Recombinant Multiprotein Complexes. Methods Enzymol. 592, 1–26. https://doi.org/10.1016/bs.mie.2017.03.008.
- Punjani, A., Rubinstein, J.L., Fleet, D.J., and Brubaker, M.A. (2017). cryoSPARC: algorithms for rapid unsupervised cryo-EM structure determination. Nat. Methods 14, 290–296. https://doi.org/10.1038/ nmeth.4169.

- Afonine, P.V., Poon, B.K., Read, R.J., Sobolev, O.V., Terwilliger, T.C., Urzhumtsev, A., and Adams, P.D. (2018). Real-space refinement in PHENIX for cryo-EM and crystallography. Acta Crystallogr. D Struct. Biol. 74, 531–544. https://doi.org/10.1107/s2059798318006551.
- Croll, T.I. (2018). ISOLDE: a physically realistic environment for model building into low-resolution electron-density maps. Acta Crystallogr. D Struct. Biol. 74, 519–530. https://doi.org/10.1107/s2059798318002425.
- Goddard, T.D., Huang, C.C., Meng, E.C., Pettersen, E.F., Couch, G.S., Morris, J.H., and Ferrin, T.E. (2018). UCSF ChimeraX: Meeting modern challenges in visualization and analysis. Protein Sci. 27, 14–25. https:// doi.org/10.1002/pro.3235.
- Dyer, P.N., Edayathumangalam, R.S., White, C.L., Bao, Y., Chakravarthy, S., Muthurajan, U.M., and Luger, K. (2004). Reconstitution of Nucleosome Core Particles from Recombinant Histones and DNA. Methods Enzymol. 375, 23–44. https://doi.org/10.1016/s0076-6879(03)75002-2.
- Mastronarde, D.N. (2003). SerialEM: A Program for Automated Tilt Series Acquisition on Tecnai Microscopes Using Prediction of Specimen Position. Microsc. Microanal. 9, 1182–1183. https://doi.org/10.1017/ s1431927603445911.
- Sanchez-Garcia, R., Gomez-Blanco, J., Cuervo, A., Carazo, J.M., Sorzano, C.O.S., and Vargas, J. (2021). DeepEMhancer: a deep learning solution for cryo-EM volume post-processing. Commun. Biol. 4, 874. https://doi.org/10.1038/s42003-021-02399-1.
- Emsley, P., Lohkamp, B., Scott, W.G., and Cowtan, K. (2010). Features and development of Coot. Acta Crystallogr. D Biol. Crystallogr. 66, 486–501. https://doi.org/10.1107/s0907444910007493.
- Evans, R., O'Neill, M., Pritzel, A., Antropova, N., Senior, A., Green, T., Žídek, A., Bates, R., Blackwell, S., Yim, J., et al. (2022). Protein complex prediction with AlphaFold-Multimer. Preprint at bioRxiv. https://doi.org/ 10.1101/2021.10.04.463034.





### **STAR**\***METHODS**

### **KEY RESOURCES TABLE**

REAGENT or RESOURCE	SOURCE	IDENTIFIER
Bacterial and virus strains		
E. coli DH5α	NEB	Cat# C2987H
E. coli DH10EMBacY	Geneva Biotech	N/A
E. coli BL21-CodonPlus (DE3)-RIL	Agilent	Cat# 230245
Chemicals, peptides, and recombinant proteins		
Phusion polymerase	This study	N/A
QIAprep Spin Miniprep Kit	Qiagen	Cat# 27106
QIAquick Gel Extraction Kit	Qiagen	Cat# 28706
ATP	Sigma-Aldrich	Cat# A5394
DTT	Bio-Rad	Cat# 1610611
RNase A	Sigma-Aldrich	Cat# R5503
SYBR Gold Nucleic Acid Gel Stain	Invitrogen	Cat# S11494
Thermo Scientific PageRuler Prestained 10 180kDa Protein Ladder	Thermo Scientific	Cat# 26617
BSA	Sigma-Aldrich	Cat #B8667
One-Step Blue Protein Gel Stain	Biotium	Cat# 21003
IPTG	Sigma-Aldrich	Cat# I5502
ESF 921 Insect Cell Culture Medium	Expression Systems	Cat# 96-001-01
Amylose resin	NEB	Cat# E8021L
Leupeptin	RPI	Cat# L22035-0.050
Pepstatin A	AdipoGen	Cat# AGCP37001M100
PMSF	RPI	Cat# P20270-25.0
Benzamidine	RPI	Cat# B12000-100.0
Adenosine 5'-diphosphate sodium salt	Sigma-Aldrich	Cat# A2754
Beryllium sulfate tetrahydrate	Sigma-Aldrich	Cat# 202789
Sodium fluoride	Sigma-Aldrich	Cat# 201154
Glutaraldehyde	EMS	Cat# 16200
Phosphoenolpyruvate	Sigma-Aldrich	Cat# 10108294001
Nicotinamide adenine dinucleotide (NADH)	Sigma-Aldrich	Cat# 481913
Pyruvate kinase/lactic dehydrogenase enzyme mix	Sigma-Aldrich	Cat# P0294
Glycerol	VWR	Cat# BDH1172
Deposited data		
CHD1-nucleosome complex (anchored state)	This study	PDB: 9NH8
CHD1-nucleosome complex (closed state)	This study	PDB: 9EAR
map A and map B (closed state)	This study	EMDB: EMD-47841
map I (closed state with exit side DBR)	This study	EMDB: EMD-47857
map C and map D (anchored state)	This study	EMDB: EMD-49406
map H (anchored state with entry side DBR)	This study	EMDB: EMD-47852
map E and map F (docked state)	This study	EMDB: EMD-47845
map G (docked state with entry side DBR)	This study	EMDB: EMD-47856
Uncropped gel images and raw data fluorescent polarization data	This study	Mendeley Data: https://doi.org/10.17632/ hdhcsf6k6m.1

(Continued on next page)

### **Article**



REAGENT or RESOURCE Experimental models: Cell lines  S121 cells Expression Systems Cattl 94-001S S19 cells Expression Systems Cattl 94-001S Tril (High cells Expression Systems Cattl 94-001S Cattl XTG9-RO  Oligonucleotides  AU001, NCP_30bpOverhang, F (CCT GTT ATT CCT AGT AAT CAA TCA GTG CCT ATC GAT GTA TAT ATC TGA CAC GTG CCT ATC GAT GTA TAT ATC TGA CAC GTG CCT ATC GAT GTA TAT ATC TGA CAC GTG CCT ATC GAT GTA TAT ATC TGA CAC GTG CCT ATC CAA CTA AAG CTT AGA TGT GCG AAT TCC AGC CAT CAG ATC CCG GTG CCC GI AU0022, NCP_30bpOverhang R (FAMW AU0024_00bp_overhang F (CTA CAT TCC AGG CAT CAG ATT CCC GCG GC CCT GTT ATT CCT TGC CGC CGG CCT GTT ATT CCT AGT AAT CAA TCA GTG CCT ATC GAT GAT TAT ATC TGA CAC GTG CCT)  AU0026_00vidom801_FAM_R (6FAM/ATC AGA ATC CCG GTG CCG)  AU0026_00vidom801_FAM_R (6FAM/ATC AGA ATC CGG GTG CCG)  AU0026_00vidom801_FAM_R (6FAM/ATC AGA ATC CCG GTG CCG)  AU0026_00vidom801_FAM_R (6FAM/ATC AGA ATC CGG GTG CCG)  Recombinant DNA  438-C_NHis6-TEV-CHD1 (10072A, This study N/A 438-C_NHis6-TEV-CHD1 (1007-1074 GSG) This study N/A 438-C_NHis6-TEV-CHD1 (1007-1074 GSG) This study N/A 438-C_NHis6-TEV-CHD1 (1732P, NT50P) This study N/A 438-C_NHis6-TEV-SMARCAS This study N/A 438-C_NHis6-TEV-CHD1 (1007-1074 GSG) This study N/A 438-C_NHis6-TEV-CHD1 (1007-1074 GSG) This study N/A 438-C_NHis6-TEV-CHD1 (10074 GSG) This study N/A 438-C_NHis6-TEV-CHD1 (	Continued		
Expression Systems		SOURCE	IDENTIFIER
Signature   Sign		GOOTIOE	IDENTIFICIT
Expression Systems		Evaragian Systems	Cat# 04 003C
Tri (HS) cells		·	
X-tremeGENE9 transfection reagent		•	
Oligonucleotides         August JNOP, 30bpOverhang, F (CCT GTT ATT ACT CAT ACT ACT ACT ACT ACT ACT A	, ,	·	
AU001_NCP_30bpOverhang_F (CCT GTT ATT CCT AGT AGT CAGT CAGT CTATC GGT GTAT ATT CAGT AGT CAGT CTATC GGT GTAT ATT ATC TGA CAG CGT CCT AU002_NCP_30bpOverhangR (6FAM/ CAC TTA AGT TGA CAG CGG CCT AU002_NCP_30bpOverhangR (6FAM/ CAC TTA AGT TGA CAGT AGG ATT TCC AGC CAT CAG AAT CCC GGT GCC G) AU002_80bp_overhang F (CTA CAT TCC AGG CAG TGC CTC TGC CGC CGG CCT GTT ATT CCT AGT AGT CAG TGC CCT AGG CAG TGC CTC TGC CGC CGG CCT GTT ATT CCT AGT AGT CAG TGC CCT ATT AGT TCC AGT CAG TGC AGG CAG TGC CTC TGC CGC CGG CCT GTT ATT ACT CGA CGT CAGT CGC AGG CGT GCCT)  AU002_80widone601_FAM_R (6FAM/ATC AGA ATC CCG GTG CCG) AU002_80widone601_FAM_R (6FAM/ATC AGA ATC CCG GTG CCG ATC CCG ATC CCG ATC CCG AGA ATC CCG GTG CCG ATC CCG		Roche	Cat# XTG9-RO
ATT COT AGT AAT CAA TCA GCTA CCTATC GAT GTA TAT ATC TGA CAC GTG CCT) AJ0002_NCP_30bpOverhangR (8FAM/ CAA CTA AAG CTT AGA TGT GCG AAT TCC AGC CAT CAG AAT CCC GGT GCC G) AJ0002_ROP_30bpOverhangR (8FAM/ CAA CTA AAG CTT AGA TGT GCG AAT TCC AGC CAT CAG AAT CCC GGT GCC G) AJ0002_ROP_30bp_overhangR (CTA CAT TCC AJ002_ROP_30bp_overhangR (CTA CAT TCC AJ002_ROP_30bp_overhangR (CTA CAT TCC AJ002_ROP_30bp_overhangR (CTA CAT TCC CAT CAT CAT CAT CAT CAT CAC GTG CCT GTT ATT CCT TAG CAT CAC GTG CCT ATT CAT CAT CAT CAT CAC AT GCAC GTG CCT) AJ002_ROW/domn601_FAM_R (8FAM/ATC AGA ATC CCG GTG CCG) AJ002_ROW/domn601_FAM_R (8FAM/ATC AGA ATC CCG GTG CCG AGA ATC CCG ATC ATC ATC ATC ATC ATC ATC ATC A			
CAA CTA AAĞ CTT AAĞ TGT GCG AAT TCC AGC CAT CAG AAT CCC GGT GCC G)  AJ0022_60bp_overhang_F (CTA CAT TCC AGG CAG TGC CTC TGC CGC CGG CCT GTT ATT CCT ACG TGT ACT CAT CCC AGG CAG TGC CTC TGC CGC CGG CCT GTT ATT CCT ACG TGT ACT CAT CAGT CCT ATC GAT GTA TAT ATC TGA CTG ACT ACG AT GTA TAT ATC TGA CTG ACC AGG AT GC CTG TGC CGG AJ0025_0Widom601_FAM_R (6FAM/ ATC AGA ATC CCG GTG CCG)  AJ0025_0Widom601_FAM_R (6FAM/ ATC AGA ATC CCG GTG CCG)  AJ0024_0Widom601_FAM_R (6FAM/ ATC AGA ATC CCG GTG CCG)  AJ0024_0Widom601_F (ATC GAT GTA TAT ATC TGA CAC GTG CCT)  Recombiant DNA  438-C_NHise-TEV-CHD1 (R1072A, This study N/A 438-C_NHise-TEV-CHD1 (1067-1074 GSG) This study N/A 438-C_NHise-TEV-CHD1 (1067-1074 GSG) This study N/A 438-C_NHise-TEV-CHD1 (R1072A, This study N/A 438-C_NHise-TEV-CHD1 (R732P, N750P) This study N/A 438-C_NHise-TEV-SMARCA5 ASS-C_NHise-TEV-SMARCA5 This study N/A 438-C_NHise-TEV-SMARCA5 This study This stud	ATT CCT AGT AAT CAA TCA GTG CCT ATC	This study	N/A
AGG CAG TGC CTG TGC CGC CGG CCT GTT ATT CCT AGT AAT CAA TCA ATCA CGT CCT ATC GAT GTA TAT ATC TGA CAC GTG CCT)  AU0025_0Widom601_FAM_R (6FAM/ATC	CAA CTA AAG CTT AGA TGT GCG AAT	This study	N/A
AGA ATC CCG GTG CCG)  AJ0024_0Widom601_F (ATC GAT GTA TAT ATC TGA CAC GTG CCT)  Recombinant DNA  438-C_NHis6-TEV-CHD1 This study N/A  438-C_NHis6-TEV-CHD1 (R1072A, This study N/A  438-C_NHis6-TEV-CHD1 (R1072A, This study N/A  438-C_NHis6-TEV-CHD1 (R1067-1074 GSG) This study N/A  438-C_NHis6-TEV-CHD1 (W1043A) This study N/A  438-C_NHis6-TEV-CHD1 (W1043A) This study N/A  438-C_NHis6-TEV-CHD1 (W1043A) This study N/A  438-C_NHis6-TEV-SMARCA5 This	AGG CAG TGC CTC TGC CGC CGG CCT GTT ATT CCT AGT AAT CAA TCA GTG CCT ATC GAT GTA TAT ATC TGA CAC	This study	N/A
### ATC TGA CAC GTG CCT)    Recombinant DNA	`	This study	N/A
438-C_NHis6-TEV-CHD1         This study         N/A           438-C_NHis6-TEV-CHD1 (R1072A, R1074A)         This study         N/A           438-C_NHis6-TEV-CHD1 (1067-1074 GSG)         This study         N/A           438-C_NHis6-TEV-CHD1 (W1043A)         This study         N/A           438-C_NHis6-TEV-SMARCA5         This study         N/A           438-C_NHis6-TEV-SMARCA5 (W730A)	_ ·	This study	N/A
438-C_NHis6-TEV-CHD1 (R1072A, R107AA)         This study         N/A           438-C_NHis6-TEV-CHD1 (1067-1074 GSG)         This study         N/A           438-C_NHis6-TEV-CHD1 (W1043A)         This study         N/A           438-C_NHis6-TEV-CHD1 (R732P, N750P)         This study         N/A           438-C_NHis6-TEV-SMARCA5         This study         N/A           438-C_NHis6-TEV-SMARCA5 (W730A)         This study         N/A           438-C_NHis6-TEV-SMARCA5 (W730	Recombinant DNA		
438-C_NHis6-TEV-CHD1 (R1072A, R1074A)         This study         N/A           438-C_NHis6-TEV-CHD1 (1067-1074 GSG)         This study         N/A           438-C_NHis6-TEV-CHD1 (W1043A)         This study         N/A           438-C_NHis6-TEV-CHD1 (R732P, N750P)         This study         N/A           438-C_NHis6-TEV-SMARCA5         This study         N/A           438-C_NHis6-TEV-SMARCA5 (W730A)         This study         N/A           438-C_NHis6-TEV-SMARCA5 (W730A)         This study         N/A           438-C_NHis6-TEV-SMARCA5 (W730A)         This study         N/A           (K430P, N448P)         N/A         Addgene #55220           Software and algorithms         Gradia et al. <sup>61</sup> Addgene #55220           Software and algorithms         Hitps://www.graphpad.com/           GraphPad Prism (version 10.2.2)         GraphPad Software Inc.         https://www.graphpad.com/           PHENIX (version 1.2.0.1)         Afonine et al. <sup>62</sup> https://www.cryosparc.com           PHENIX (version 1.2.0.1)         Afonine et al. <sup>63</sup> https://www.cryosparc.com           PHENIX (version 1.6.0)         Croll <sup>64</sup> https://www.cryosparc.com           UCSF ChimeraX (versions 1.5-1.6)         Goddard et al. <sup>65</sup> https://www.cgl.ucsf.edu/chimeraX/           Adobe Illustrator (version 25.4	438-C_NHis6-TEV-CHD1	This study	N/A
438-C_NHis6-TEV-CHD1 (W1043A)         This study         N/A           438-C_NHis6-TEV-CHD1 (R732P, N750P)         This study         N/A           438-C_NHis6-TEV-SMARCA5         This study         N/A           438-C_NHis6-TEV-SMARCA5 (W730A)         This study         N/A           438-C_NHis6-TEV-SMARCA5 (W730A)         This study         N/A           (K430P, N448P)         N/A         N/A           438-C         Gradia et al. <sup>61</sup> Addgene #55220           Software and algorithms           GraphPad Prism (version 10.2.2)         GraphPad Software Inc.         https://www.graphpad.com/           CryoSPARC (v3.3.2 and v4.6.0)         Punjani et al. <sup>62</sup> https://www.cryosparc.com           PHENIX (version 1.20.1)         Afonine et al. <sup>63</sup> https://phenix-online.org/           ISOLDE (version 1.6.0)         Croll <sup>64</sup> https://phenix-online.org/           UCSF ChimeraX (versions 1.5-1.6)         Goddard et al. <sup>65</sup> https://www.cgl.ucsf.edu/chimerax/           Adobe Illustrator (version 25.4.1)         Adobe         https://www.adobe.com/products/illustrator.html           Other           HiLoad 16/600 Superdex 200 pg column         Cytiva         Cat# 28989335           Superose 6		•	N/A
438-C_NHis6-TEV-CHD1 (R732P, N750P)         This study         N/A           438-C_NHis6-TEV-SMARCA5         This study         N/A           438-C_NHis6-TEV-SMARCA5 (W730A)         This study         N/A           438-C_NHis6-TEV-SMARCA5         This study         N/A           (K430P, N448P)         N/A           438-C_SMARCA5         This study         N/A           50ftware and algorithms         Addgene #55220           GraphPad Prism (version 10.2.2)         GraphPad Software Inc.         https://www.graphpad.com/           cryoSPARC (v3.3.2 and v4.6.0)         Punjani et al. <sup>62</sup> https://www.cryosparc.com           PHENIX (version 1.20.1)         Afonine et al. <sup>63</sup> https://www.cryosparc.com           PHENIX (version 1.6.0)         Croll <sup>64</sup> https://tristanic.github.io/isolde/           UCSF ChimeraX (versions 1.5-1.6)         Goddard et al. <sup>65</sup> https://tristanic.github.io/isolde/           UCSF ChimeraX (versions 25.4.1)         Adobe         https://www.cgl.ucsf.edu/chimerax/           Adobe Illustrator (version 25.4.1)         Adobe         https://www.adobe.com/products/illustrator.html           Other           HiLoad 16/600 Superdex 200 pg column         Cytiva         Cat# 28989335           Superose 6 Increase 10/300 GL column         Cytiva <t< td=""><td>438-C_NHis6-TEV-CHD1 (1067-1074 GSG)</td><td>This study</td><td>N/A</td></t<>	438-C_NHis6-TEV-CHD1 (1067-1074 GSG)	This study	N/A
438-C_NHis6-TEV-SMARCA5         This study         N/A           438-C_NHis6-TEV-SMARCA5 (W730A)         This study         N/A           438-C_NHis6-TEV-SMARCA5         This study         N/A           438-C_NHis6-TEV-SMARCA5         This study         N/A           438-C_NHis6-TEV-SMARCA5         This study         N/A           438-C_SARCA5         This study         N/A           438-C_NHis6-TEV-SMARCA5         This study         N/A           438-C_NHis6-TEV-SMARCA5         This study         N/A           438-C_NHis6-TEV-SMARCA5         N/A         N/A           848-C_NHis6-TEV-SMARCA5         N/A         N/A           65         N/A         N/A         N/A           66         N/A         N/A         N/A           67         N/A         N/A         N/A         N/A           68         N/A         N/A         N/A         N/A         N/A           69         N/A         N/A         N/A	438-C_NHis6-TEV-CHD1 (W1043A)	This study	N/A
438-C_NHis6-TEV-SMARCA5 (W730A)         This study         N/A           438-C_NHis6-TEV-SMARCA5 (K430P, N448P)         This study         N/A           438-C_NHis6-TEV-SMARCA5 (K430P, N448P)         Gradia et al. <sup>61</sup> Addgene #55220           Software and algorithms           GraphPad Prism (version 10.2.2)         GraphPad Software Inc.         https://www.cgaphpad.com/           cryoSPARC (v3.3.2 and v4.6.0)         Punjani et al. <sup>62</sup> https://www.cgnaphpad.com/           PHENIX (version 1.20.1)         Afonine et al. <sup>63</sup> https://www.cyosparc.com           PHENIX (version 1.6.0)         Croll <sup>64</sup> https://phenix-online.org/           ISOLDE (version 1.6.0)         Croll <sup>64</sup> https://phenix-online.org/           UCSF ChimeraX (versions 1.5-1.6)         Goddard et al. <sup>65</sup> https://www.cgl.ucsf.edu/chimerax/           Adobe Illustrator (version 25.4.1)         Adobe         https://www.adobe.com/products/           Adobe Illustrator (version 25.4.1)         Catil 28989335           Superose 6 Increase 10/300 GL column         Cytiva         Catil 28989335           Superose 6 Increase 3.2/300         Cytiva         Catil 29091598           HisTrap HP column         Cytiva         Catil 28988937	438-C_NHis6-TEV-CHD1 (R732P, N750P)	This study	N/A
438-C_NHis6-TEV-SMARCA5 (K430P, N448P)  438-C Gradia et al. 61 Addgene #55220  Software and algorithms  GraphPad Prism (version 10.2.2) GraphPad Software Inc. https://www.graphpad.com/ cryoSPARC (v3.3.2 and v4.6.0) Punjani et al. 62 https://www.cryosparc.com PHENIX (version 1.20.1) Afonine et al. 63 https://phenix-online.org/ ISOLDE (version 1.6.0) Croll 64 https://tristanic.github.io/isolde/ UCSF ChimeraX (versions 1.5-1.6) Goddard et al. 65 https://www.cgl.ucsf.edu/chimerax/ Adobe Illustrator (version 25.4.1) Adobe https://www.adobe.com/products/ illustrator.html  Other  HiLoad 16/600 Superdex 200 pg column Cytiva Cat# 28989335 Superose 6 Increase 10/300 GL column Cytiva Cat# 29091598  HisTrap HP column Cytiva Cat# 29091598  HisTrap HP column Cytiva Cat# 29091598  KK column 16/20 column Cytiva Cat# 28988937  Typhoon 5 GE Healthcare N/A  NuPAGE 4-12% Bis-Tris protein gels Invitrogen Cat# NP0321BOX	438-C_NHis6-TEV-SMARCA5	This study	N/A
(K430P, N448P)           438-C         Gradia et al. 61         Addgene #55220           Software and algorithms           GraphPad Prism (version 10.2.2)         GraphPad Software Inc.         https://www.graphpad.com/           cryoSPARC (v3.3.2 and v4.6.0)         Punjani et al. 62         https://www.cryosparc.com           PHENIX (version 1.20.1)         Afonine et al. 63         https://phenix-online.org/           ISOLDE (version 1.6.0)         Croll 64         https://tristanic.github.io/isolde/           UCSF ChimeraX (versions 1.5-1.6)         Goddard et al. 65         https://www.cgl.ucsf.edu/chimerax/           Adobe Illustrator (version 25.4.1)         Adobe         https://www.adobe.com/products/illustrator.html           Other           HiLoad 16/600 Superdex 200 pg column         Cytiva         Cat# 28989335           Superose 6 Increase 10/300 GL column         Cytiva         Cat# 29091596           Superose 6 Increase 3.2/300         Cytiva         Cat# 29091598           HisTrap HP column         Cytiva         Cat# 27524802           XK column 16/20 column         Cytiva         Cat# 28988937           Typhoon 5         GE Healthcare         N/A           NuPAGE 4-12% Bis-Tris protein gels         Invitrogen         Cat# NP0321BOX	438-C_NHis6-TEV-SMARCA5 (W730A)	This study	N/A
Software and algorithms  GraphPad Prism (version 10.2.2) GraphPad Software Inc. https://www.graphpad.com/ cryoSPARC (v3.3.2 and v4.6.0) Punjani et al. 62 https://www.cryosparc.com PHENIX (version 1.20.1) Afonine et al. 63 https://phenix-online.org/ ISOLDE (version 1.6.0) Croll 64 https://tristanic.github.io/isolde/ UCSF ChimeraX (versions 1.5-1.6) Goddard et al. 65 https://www.cgl.ucsf.edu/chimerax/ Adobe Illustrator (version 25.4.1) Adobe https://www.adobe.com/products/ illustrator.html  Other  HiLoad 16/600 Superdex 200 pg column Cytiva Cat# 28989335 Superose 6 Increase 10/300 GL column Cytiva Cat# 29091596 Superose 6 Increase 3.2/300 Cytiva Cat# 29091598 HisTrap HP column Cytiva Cat# 17524802 XK column 16/20 column Cytiva Cat# 28988937 Typhoon 5 GE Healthcare N/A NuPAGE 4-12% Bis-Tris protein gels Invitrogen Cat# NP0321BOX	438-C_NHis6-TEV-SMARCA5 (K430P, N448P)	This study	N/A
GraphPad Prism (version 10.2.2) GraphPad Software Inc. https://www.graphpad.com/ cryoSPARC (v3.3.2 and v4.6.0) Punjani et al. 62 https://www.cryosparc.com PHENIX (version 1.20.1) Afonine et al. 63 https://phenix-online.org/ ISOLDE (version 1.6.0) Croll 64 https://tristanic.github.io/isolde/ UCSF ChimeraX (versions 1.5-1.6) Goddard et al. 65 https://www.cgl.ucsf.edu/chimerax/ Adobe Illustrator (version 25.4.1) Adobe https://www.adobe.com/products/ illustrator.html  Other  HiLoad 16/600 Superdex 200 pg column Cytiva Cat# 28989335 Superose 6 Increase 10/300 GL column Cytiva Cat# 29091596 Superose 6 Increase 3.2/300 Cytiva Cat# 29091598 HisTrap HP column Cytiva Cat# 29091598  Cat# 17524802 XK column 16/20 column Cytiva Cat# 28988937 Typhoon 5 GE Healthcare N/A NuPAGE 4-12% Bis-Tris protein gels Invitrogen Cat# NP0321BOX	438-C	Gradia et al. <sup>61</sup>	Addgene #55220
GraphPad Prism (version 10.2.2) GraphPad Software Inc. https://www.graphpad.com/ cryoSPARC (v3.3.2 and v4.6.0) Punjani et al. 62 https://www.cryosparc.com PHENIX (version 1.20.1) Afonine et al. 63 https://phenix-online.org/ ISOLDE (version 1.6.0) Croll 64 https://tristanic.github.io/isolde/ UCSF ChimeraX (versions 1.5-1.6) Goddard et al. 65 https://www.cgl.ucsf.edu/chimerax/ Adobe Illustrator (version 25.4.1) Adobe https://www.adobe.com/products/ illustrator.html  Other  HiLoad 16/600 Superdex 200 pg column Cytiva Cat# 28989335 Superose 6 Increase 10/300 GL column Cytiva Cat# 29091596 Superose 6 Increase 3.2/300 Cytiva Cat# 29091598 HisTrap HP column Cytiva Cat# 29091598  Cat# 17524802 XK column 16/20 column Cytiva Cat# 28988937 Typhoon 5 GE Healthcare N/A NuPAGE 4-12% Bis-Tris protein gels Invitrogen Cat# NP0321BOX	Software and algorithms		
cryoSPARC (v3.3.2 and v4.6.0) Punjani et al. 62 https://www.cryosparc.com PHENIX (version 1.20.1) Afonine et al. 63 https://phenix-online.org/ ISOLDE (version 1.6.0) Croll 4 https://tristanic.github.io/isolde/ UCSF ChimeraX (versions 1.5-1.6) Goddard et al. 65 https://www.cgl.ucsf.edu/chimeraX/ Adobe Illustrator (version 25.4.1) Adobe https://www.adobe.com/products/ iillustrator.html  Other  HiLoad 16/600 Superdex 200 pg column Cytiva Cat# 28989335 Superose 6 Increase 10/300 GL column Cytiva Cat# 29091596 Superose 6 Increase 3.2/300 Cytiva Cat# 29091598 HisTrap HP column Cytiva Cat# 17524802 XK column 16/20 column Cytiva Cat# 28988937 Typhoon 5 GE Healthcare N/A NuPAGE 4-12% Bis-Tris protein gels Invitrogen Cat# NP0321BOX		GraphPad Software Inc.	https://www.graphpad.com/
PHENIX (version 1.20.1)  Afonine et al. 63  https://phenix-online.org/  ISOLDE (version 1.6.0)  UCSF ChimeraX (versions 1.5-1.6)  Adobe Illustrator (version 25.4.1)  Adobe Illustrator (version 25.4.1)  Adobe https://www.adobe.com/products/illustrator.html  Other  HiLoad 16/600 Superdex 200 pg column  Cytiva  Cat# 28989335  Superose 6 Increase 10/300 GL column  Cytiva  Cat# 29091596  Superose 6 Increase 3.2/300  Cytiva  Cat# 29091598  HisTrap HP column  Cytiva  Cat# 29091598  HisTrap HP column  Cytiva  Cat# 29091598  Cat# 17524802  XK column 16/20 column  Cytiva  Cat# 28988937  Typhoon 5  GE Healthcare  N/A  NuPAGE 4-12% Bis-Tris protein gels  Invitrogen  Cat# NP0321BOX	,	•	
ISOLDE (version 1.6.0)  Croll <sup>64</sup> Mttps://tristanic.github.io/isolde/ UCSF ChimeraX (versions 1.5-1.6)  Goddard et al. <sup>65</sup> https://www.cgl.ucsf.edu/chimerax/ Adobe Illustrator (version 25.4.1)  Adobe  https://www.adobe.com/products/ illustrator.html  Other  HiLoad 16/600 Superdex 200 pg column  Cytiva  Cat# 28989335  Superose 6 Increase 10/300 GL column  Cytiva  Cat# 29091596  Superose 6 Increase 3.2/300  Cytiva  Cat# 29091598  HisTrap HP column  Cytiva  Cat# 29091598  KK column 16/20 column  Cytiva  Cat# 28988937  Typhoon 5  GE Healthcare  N/A  NuPAGE 4-12% Bis-Tris protein gels  Invitrogen  Cat# NP0321BOX		•	
UCSF ChimeraX (versions 1.5-1.6)  Adobe Illustrator (version 25.4.1)  Adobe Illustrator (version 25.4.1)  Adobe Illustrator (version 25.4.1)  Other  HiLoad 16/600 Superdex 200 pg column  Cytiva  Cat# 28989335  Superose 6 Increase 10/300 GL column  Cytiva  Cat# 29091596  Superose 6 Increase 3.2/300  Cytiva  Cat# 29091598  HisTrap HP column  Cytiva  Cat# 29091598  KK column 16/20 column  Cytiva  Cat# 28988937  Typhoon 5  GE Healthcare  N/A  NuPAGE 4-12% Bis-Tris protein gels  Invitrogen  Adobe  https://www.cgl.ucsf.edu/chimerax/  https://www.adobe.com/products/ illustrator.html  Cat# 28989335  Cat# 28988937  N/A  NuPAGE 4-12% Bis-Tris protein gels  Invitrogen			
Adobe Illustrator (version 25.4.1)  Adobe  https://www.adobe.com/products/illustrator.html  Other  HiLoad 16/600 Superdex 200 pg column  Cytiva  Cat# 28989335  Superose 6 Increase 10/300 GL column  Cytiva  Cat# 29091596  Superose 6 Increase 3.2/300  Cytiva  Cat# 29091598  HisTrap HP column  Cytiva  Cat# 17524802  XK column 16/20 column  Cytiva  Cat# 28988937  Typhoon 5  GE Healthcare  N/A  NuPAGE 4-12% Bis-Tris protein gels  Invitrogen  Adobe  https://www.adobe.com/products/illustrator.html	· · ·		
HiLoad 16/600 Superdex 200 pg column         Cytiva         Cat# 28989335           Superose 6 Increase 10/300 GL column         Cytiva         Cat# 29091596           Superose 6 Increase 3.2/300         Cytiva         Cat# 29091598           HisTrap HP column         Cytiva         Cat# 17524802           XK column 16/20 column         Cytiva         Cat# 28988937           Typhoon 5         GE Healthcare         N/A           NuPAGE 4-12% Bis-Tris protein gels         Invitrogen         Cat# NP0321BOX	Adobe Illustrator (version 25.4.1)		https://www.adobe.com/products/
Superose 6 Increase 10/300 GL column         Cytiva         Cat# 29091596           Superose 6 Increase 3.2/300         Cytiva         Cat# 29091598           HisTrap HP column         Cytiva         Cat# 17524802           XK column 16/20 column         Cytiva         Cat# 28988937           Typhoon 5         GE Healthcare         N/A           NuPAGE 4-12% Bis-Tris protein gels         Invitrogen         Cat# NP0321BOX	Other		
Superose 6 Increase 10/300 GL column         Cytiva         Cat# 29091596           Superose 6 Increase 3.2/300         Cytiva         Cat# 29091598           HisTrap HP column         Cytiva         Cat# 17524802           XK column 16/20 column         Cytiva         Cat# 28988937           Typhoon 5         GE Healthcare         N/A           NuPAGE 4-12% Bis-Tris protein gels         Invitrogen         Cat# NP0321BOX	HiLoad 16/600 Superdex 200 pa column	Cytiva	Cat# 28989335
Superose 6 Increase 3.2/300 Cytiva Cat# 29091598 HisTrap HP column Cytiva Cat# 17524802 XK column 16/20 column Cytiva Cat# 28988937 Typhoon 5 GE Healthcare N/A NuPAGE 4-12% Bis-Tris protein gels Invitrogen Cat# NP0321BOX	, , , ,	•	
HisTrap HP column Cytiva Cat# 17524802  XK column 16/20 column Cytiva Cat# 28988937  Typhoon 5 GE Healthcare N/A  NuPAGE 4-12% Bis-Tris protein gels Invitrogen Cat# NP0321BOX	·	•	
XK column 16/20 column Cytiva Cat# 28988937  Typhoon 5 GE Healthcare N/A  NuPAGE 4-12% Bis-Tris protein gels Invitrogen Cat# NP0321BOX	•	•	
Typhoon 5 GE Healthcare N/A NuPAGE 4-12% Bis-Tris protein gels Invitrogen Cat# NP0321BOX		•	
NuPAGE 4-12% Bis-Tris protein gels Invitrogen Cat# NP0321BOX		•	
		<u>.</u>	

(Continued on next page)



Continued		
REAGENT or RESOURCE	SOURCE	IDENTIFIER
Titan Krios + K3 + GATAN GIF Filter	FEI/Thermo Fisher Scientific/ GATAN	N/A
Greiner Bio-One Small Volume 384 Well HiBase Polypropylene Microplates	Greiner Bio-One	Cat# 784076-25
Corning 384-Well Clear Polystyrene Microplates	Sigma-Aldrich	Cat# CLS3702BC
Amicon 15 ml 100,000 MWCO spin concentrator	Merck	Cat# UFC910008
Quantifoil Holey Carbon Films, R 2/1	Quantifoil Micro Tools	Cat #Q250-CR1

#### **EXPERIMENTAL MODEL AND STUDY PARTICIPANT DETAILS**

#### **Cell culture**

Sf9 cells (Expression Systems, Cat# 94-001S), Tni (Hi5) cells (Expression Systems, Cat# 94-002S), and Sf21 cells (Expression Systems, Cat# 94-003S) were cultured in ESF 921 insect cell culture medium (Expression Systems, Cat# 96-001-01) at  $27^{\circ}$ C for baculovirus production and protein expression, unless otherwise indicated. E. coli DH5 $\alpha$  (New England Biolabs (NEB) Cat# C2987H), DH10EMBacY (Geneva Biotech), and BL21-CodonPlus (DE3)-RIL (Agilent Cat# 230245) were cultured in LB broth (EMD-Millipore Cat# 71753-5) at  $37^{\circ}$ C for plasmid production and protein expression, unless otherwise indicated.

### **METHOD DETAILS**

#### **Cloning & mutagenesis**

*H. sapiens* CHD1 (residues 1-1327, referred to as CHD1 throughout) and full-length *H. sapiens* SMARCA5 were cloned into ligation independent cloning-compatible vectors from cDNA. Mutations were introduced by sequence- and ligation independent cloning or 'Round-The-Horn mutagenesis. CHD1 and SMARCA5 were cloned into the 438 series of vectors with a tobacco etch virus protease-cleavable N-terminal His6-MBP-Asn10-TEV tag.<sup>61</sup> All plasmids were sequence verified by long-read sequencing.

### **Protein expression**

*H. sapiens* CHD1 and *H. sapiens* SMARCA5 and their mutants were expressed in insect cells. <sup>29</sup> Bacmid, virus, and protein production were performed as previously described. <sup>28</sup> To generate bacmids, expression plasmids (438-C with the appropriate ORF) were electroporated into DH10EMBacY cells. All insect cells were grown in ESF921 medium at 27°C and were harvested 72 hr after transfection or infection. To generate V0 virus, bacmids were transfected into Sf9 cells using X-tremeGENE9 transfection reagent. To produce V1 virus, 25 ml of Sf21 cells were infected with 200  $\mu$ l of V0 virus. For large-scale protein expression, 600 ml of Hi5 cells were infected with 800  $\mu$ l of V1. Cells were harvested by centrifugation (240 g, 4°C, 30 min), resuspended in lysis buffer (300 mM NaCl, 20 mM Na · HEPES pH 7.4, 10% glycerol (v/v), 1 mM DTT, 30 mM imidazole pH 8.0) supplemented with protease inhibitors (final concentration of 0.284  $\mu$ g/ml leupeptin, 1.37  $\mu$ g/ml pepstatin A, 0.17 mg/ml PMSF and 0.33 mg/ml benzamidine), flash-frozen, and stored at -80°C.

X. laevis histones were expressed and purified as described.<sup>28</sup>

### **Protein purification**

CHD1, SMARCA5, and their mutants have an N-terminal His6 tag, MBP tag and TEV protease cleavage site and were purified at 4°C. The same purification was performed for wild-type CHD1, SMARCA5, and all mutants. Hi5 cells expressing CHD1 or SMARCA5 were resuspended in lysis buffer (300 mM NaCl, 20 mM Na·HEPES pH 7.4 at 25°C at 25°C, 10% (v/v) glycerol, 30 mM imidazole, 1 mM TCEP, 0.284 μg/ml leupeptin, 1.37 μg/ml pepstatin A, 0.17 mg/ml PMSF and 0.33 mg/ml benzamidine) and subsequently lysed by sonication. The lysate was centrifuged and cleared by ultra-centrifugation. The supernatant containing CHD1 or SMARCA5 was subsequently filtered using 0.22 μm syringe filters. The filtered supernatant was applied to a HisTrap HP 5 mL (Cytiva). The column was subsequently washed with 10 CV lysis buffer, 3 CV high salt buffer (1000 mM NaCl, 20 mM Na·HEPES pH 7.4 at 25°C, 10% (v/v) glycerol, 30 mM imidazole, 1 mM TCEP, 0.284 μg/ml leupeptin, 1.37 μg/ml pepstatin A, 0.17 mg/ml PMSF and 0.33 mg ml–1 benzamidine), and 5 CV lysis buffer. A self-packed XK column (Cytiva) with 15 mL of Amylose resin (New England Biolabs) was attached to the HisTrap column. CHD1 was eluted from the HisTrap column using nickel elution buffer (300 mM NaCl, 20 mM Na·HEPES pH 7.4 at 25°C, 10% (v/v) glycerol, 500 mM imidazole, 1 mM TCEP, 0.284 μg/ml leupeptin, 1.37 μg/ml pepstatin A, 0.17 mg/ml PMSF and 0.33 mg/ml benzamidine). The HisTrap column was removed, and the amylose column was washed with 5 CV lysis buffer. CHD1 or SMARCA5 was eluted from the amylose column with 5 CV amylose elution buffer (300 mM NaCl, 20 mM Na·HEPES pH 7.4 at 25°C, 10% (v/v) glycerol, 30 mM imidazole, 116.9 mM maltose, 1 mM TCEP, 0.284 μg/ml leupeptin, 1.37 μg/ml pepstatin A, 0.17 mg/ml pepstatin A, 0.17 mg/ml benzamidine). The elution was fractionated and analyzed using SDS-PAGE. Fractions containing

### **Article**



CHD1 or SMARCA5 were pooled and applied to dialysis in dialysis buffer overnight (300 mM NaCl, 20 mM Na·HEPES pH 7.4 at  $25^{\circ}$ C, 10% (v/v) glycerol, 30 mM imidazole, 1 mM TCEP, 1 mM manganese (II) chloride, 0.284 µg/ml leupeptin, 1.37 µg/ml pepstatin A, 0.17 mg/ml PMSF and 0.33 mg/ml benzamidine). 1.5 mg of TEV protease and 0.37 µg lambda protein phosphatase were added to the sample prior to dialysis to remove the N-terminal His6-MBP-Asn10 tag and dephosphorylate the protein.

The dialyzed sample was applied to a HisTrap HP 5 mL, pre-equilibrated in lysis buffer. The flow-through containing CHD1 or SMARCA5 was collected and subsequently concentrated using an Amicon 100,000 MWCO centrifugal filter unit (Millipore). The concentrated sample was applied to a Superose 6 Increase 10/300 GL (Cytiva), equilibrated in gel filtration buffer (300 mM NaCl, 20 mM Na·HEPES pH 7.4 at 25°C, 10% (v/v) glycerol, 1 mM TCEP). The elution was fractionated and analyzed by SDS-PAGE. Sample containing CHD1 was concentrated using Amicon 100,000 MWCO centrifugal filter unit (Millipore). All concentrated samples were subsequently aliquoted, flash-frozen, and stored at -80 °C prior for future use.

### Octamer formation and nucleosome reconstitution

All histone proteins were derived from *X. laevis* and refolding of histone octamers was performed as described. DNA fragments for nucleosome reconstitution were generated by PCR. <sup>29</sup> A vector containing the Widom 601 sequence was used as a template for PCR. Large-scale PCR reactions were performed with two PCR primers (Structural studies: forward primer: 5'-CCT GTT ATT CCT AGT AAT CAA TCA GTG CCT ATC GAT GTA TAT ATC TGA CAC GTG CCT-3', reverse primer: 5'-6FAM/ CAA CTA AAG CTT AGA TGT GCG AAT TCC AGC CAT CAG AAT CCC GGT GCC G-3'; Biochemical assays: forward primer: 5'-CTA CAT TCC AGG CAG TGC CTC TGC CGC CGG CCT GTT ATT CCT AGT AAT CAA TCA GTG CCT ATC GAT GTA TAT ATC TGA CAC GTG CCT-3', reverse primer: 5'-6FAM/ ATC AGA ATC CCG GTG CCG-3'); Fluorescent polarization assay without extranucleosomal DNA (Figure 2H): forward primer: 5'-ATC GAT GTA TAT ATC TGA CAC GTG CCT-3', reverse primer: 5'-6FAM/ ATC AGA ATC CCG GTG CCG-3' at a scale of 25 mL. Nucleosome core particle reconstitution was performed using the salt-gradient dialysis method. <sup>66</sup> Quantification of the reconstituted nucleosome was achieved by measuring absorbance at 280 nm. Molar extinction coefficients at 280 nm were determined for protein and nucleic acid components and were summed to yield a molar extinction coefficient for the reconstituted extended nucleosome. Nucleosomes are fluorescently labelled as indicated by the primers used to generate the nucleosomal DNA substrates.

### **Nucleosome sliding assay**

Nucleosome sliding assays were performed using 200 nM of indicated protein, 100 nM NCP with 60 base pairs extranucleosomal DNA on one side of the nucleosomal substrate, 1 mM ATP, 30 mM NaCl, 20 mM HEPES, pH 7.4 at 25°C, 0.1 mg/mL BSA, 1 mM DTT and 10% (v/v) glycerol. Reactions were incubated at 25°C and 2 µl of reaction was quenched with 10 µl quench buffer (212 ng/µL competitor DNA, 30 mM NaCl, 20 mM HEPES, pH 7.4 at 25°C, 0.1 mg/mL BSA, 1 mM DTT, and 15% (v/v) glycerol) at the indicated timepoints. 4 µL of each reaction was run on a 5% TBE gel equilibrated in 0.2x TBE running buffer at 4°C and visualized at 488 nm/530 nm using a Typhoon imager (GE Healthcare). All experiments were conducted in triplicate. Rates were calculated based on the slope after fitting the first minute of the sliding reactions via linear regression.

### **NADH-coupled ATP hydrolysis assay**

 $50 \,\mu\text{L}$  reactions were carried out in a 384-well clear microplate (Sigma-Aldrich CLS3702BC) containing 500 nM of the indicated protein, 1 mM phosphoenolpyruvate (PEP), 1 mM nicotinamide adenine dinucleotide (NADH), 100 nM NCP (30W30), 5 mM ATP and 1% (v/v) pyruvate kinase/lactic dehydrogenase enzyme mix (Sigma-Aldrich P0294) in 1X buffer (50mM Na·HEPES pH 7.4 at 25°C, 30 mM NaCl, 3 mM MgCl<sub>2</sub>, 1 mM DTT, and 10% (v/v) glycerol). ATP was added last and absorbance was read at 340 nm every 10-20 s on a Tecan SPARK plate reader at 25°C. Experiments were conducted in triplicate. Rates were calculated based on the slope after fitting the first minute of the reactions to a linear regression. Error bars represent standard deviations.

### Fluorescence polarization affinity measurement assay

CHD1 was serially diluted in gel filtration buffer (300 mM NaCl, 20 mM Na·HEPES pH 7.4 at 25°C, 10% (v/v) glycerol, 1 mM TCEP). Nucleosomes (canonical or H3K4Cme3 nucleosomes with 30 base pairs of extranucleosomal DNA on both sides or canonical nucleosomes with 0 base pairs of extranucleosomal DNA and a 5'6-FAM label on one DNA strand) at 10 nM final concentration and CHD1 (0–2  $\mu$ M final concentration) were mixed on ice in buffer containing 30 mM NaCl, 20 mM Na·HEPES pH 7.4 at 25°C, 4% (v/v) glycerol, 3 mM MgCl2, 10 $\mu$ g/mL BSA, and 2.5 mM DTT in a final volume of 30  $\mu$ l and incubated for 30 min. For experiments containing ADP·BeF<sub>3</sub>, the sample buffer was supplemented with 0.5 mM ADP·BeF<sub>3</sub>.

Fluorescence anisotropy was measured in a Greiner 384 Flat Bottom Black Small volume plate at room temperature with a Tecan SPARK multimode microplate reader with an excitation wavelength of 470 nm (±5 nm), an emission wavelength of 518 nm (±20 nm), high gain, and 100 flashes/read.

### **Complex formation for cryo-EM**

CHD1-NCP complexes were formed by incubating  $4.5~\mu M$  CHD1,  $1.5~\mu M$  H3K4Cme3 NCP, and then 1 mM ADP·BeF $_3$  in buffer containing 30 mM NaCl, 20 mM HEPES, 4% glycerol, 3 mM MgCl2, and 1 mM TCEP on ice for 20 mins. The sample was then centrifuged at 21,000 rcf and  $4^{\circ}$ C for 10 mins to remove any aggregate. The complex was purified by size-exclusion chromatography



using a Superose 6 Increase 3.2/300 column in buffer containing 30 mM NaCl, 20 mM HEPES, 4% glycerol, 3 mM MgCl2, and 1 mM TCEP. The elution was fractionated in  $50\,\mu\text{L}$  fractions and peak fractions were analyzed by Native-PAGE (5% TBE). Relevant fractions containing CHD1-bound nucleosome core particles were selected and cross-linked with 0.1% (v/v) glutaraldehyde. The crosslinking reaction was performed for 10 min on ice and subsequently quenched for 10 min using a final concentration of 2 mM lysine and 8 mM aspartate. The sample was transferred to a Slide-A-Lyzer MINI Dialysis Unit 20,000 MWCO (Thermo Scientific) and dialyzed for 2 hours against 600 ml dialysis buffer (30 mM NaCl, 3 mM MgCl2, 20 mM Na·HEPES pH 7.4, 20 mM Tris·HCl pH 7.5, 1 mM DTT).

### Sample preparation for cryo-EM

CHD1-NCP complexes were frozen on Quantifoil R2/1 on 200 Mesh Copper grids that were glow discharged for 30 s at 15 mA with 10s hold time using a Pelco Easiglow plasma discharge system.  $2\,\mu\text{L}$  of sample were applied on each side of the grid, incubated for 8 s, blotted with Ted Pella standard Vitrobot filter paper for 4 s with blot force 10 and vitrified by plunging into liquid ethane using a Vitrobot Mark IV (FEI Company), operated at 5°C and 100 % humidity.

### Cryo-EM data collection & analysis

Grids were imaged and data was collected on a Thermo Fisher Scientific Titan Krios operated at 300 keV equipped with a Gatan BioQuantum GIF and a Gatan K3 direct electron detector. Data acquisition was automated using SerialEM (v3.8.6) software <sup>67</sup> at a nominal magnification of 105,000x, corresponding to a pixel size of 0.83 Å in nanoprobe EFTEM mode. Movies consisting of 50 frames were collected in counted mode with 1.392 s exposure time and total exposure of 54.6 e<sup>-</sup>/Å.<sup>2</sup>

Image processing and analysis were performed with cryoSPARC (v3.3.2 and v4.6.0). Movies were aligned using patch motion correction followed by contrast transfer function (CTF) estimation in cryoSPARC. Particles were picked by blob-based automatic picking, resulting in 6,453,730 particles from 23,129 micrographs. Particles were extracted with a box size of 300<sup>2</sup> pixels. All classifications and refinements were conducted in cryoSPARC. Initial 2D classification was used to select particles containing nucleosome-like density. A subset of the selected particles was used to generate ab-initio volumes of CHD1-bound nucleosome and nucleosome alone. Heterogeneous refinements were used to sort CHD1-bound nucleosomes from unbound nucleosomes. Upon heterogeneous refinements of CHD1-bound nucleosome, distinct classes representing different CHD1 conformations were obtained. Heterogeneous refinements using two input volumes from each class were able to successfully sort out closed state particles (map B). Weak density was visible where the DBR would be expected to bind in the closed state. This region was low pass filtered and segmented in UCSF ChimeraX. A mask was generated by expanding the area of interest and used as an input for 3D classification to generate a map with density corresponding to the DBR (map J).

Due to similarity between the overall conformations of the anchored and docked states, 3D variability analysis was necessary to sort these states apart. The most extreme volumes from principal component 0 were used as input volumes for heterogeneous refinement. Heterogeneous refinement revealed the docked and anchored conformations as well as free nucleosomes. These volumes from a subset of the data were used as input volumes for heterogeneous refinement using all particles selected from 2D classification. A subsequent round of heterogeneous refinement revealed a class of 361,753 particles containing the anchor element at high-resolution. 3D classification was performed on these particles and revealed separate classes for the anchored and docked states. Low-resolution density was also observed near the entry-side DNA, and a 3D classification masked around entry-side DNA revealed a class of particles containing CHD1 in the anchored conformation with density for the DNA-binding region bound to the entry-side DNA, which was refined by homogeneous refinement to 3.5 Å (45,520 particles) and post-processed using deepEMhancer after filtering to the volume to 5 Å (map H). The volume consisting of CHD1 in the anchored conformation from the unmasked 3D classification was refined using non-uniform refinement to 3.2 Å (map D, 67,512 particles) and post-processed using deepEMhancer after filtering to the volume to 4 Å (map C). The docked state volume (60,216 particles) was further processed by unmasked 3D classification as well as 3D classification masked around ATPase lobe 2. The 3D classifications reveled mobility of ATPase lobe 2. A class of 21,168 particles from the unmasked classification revealed the most stable positioning of ATPase lobe 2 and was refined by homogeneous refinement to 3.8 Å (map F) and post-processed using deepEMhancer after filtering to the volume to 4.4 Å (map E). The masked 3D classification revealed a class of the docked state with density for on the entry-side DNA and was refined by homogeneous refinement to 3.9 Å (16,853 particles) and post-processed using deepEMhancer after filtering to the volume to 6 Å (map G). DeepEMhancer map sharpening<sup>68</sup> was performed in cryoSPARC for all maps and the tightTarget model was used for all post-processing steps. Volumes employed for masking of areas of interest were generated by low-pass filtering the regions of interest to 25 Å and then expanding the volume containing the area of interest by 3-5 hard pixels and 3-7 soft pixels.

Maps B, D, and F were used to build the H4 tail in each state as sharpening resulted in loss of these densities. Local resolution estimation was performed in cryoSPARC using a FSC threshold of 0.143 and local resolution visualization was performed in UCSF ChimeraX.

### Model building & refinement

For each state, AlphaFold2 models of the CHD1 double chromodomain derived from AF-014646-F1 (residues 272-454), ATPase lobe 1 (residues 455-698), ATPase lobe 2 (residues 699-729; 751-1020), gating helix (residues 730-750) and anchor element (residues 1043-1076) were placed into the densities as rigid bodies using USCF ChimeraX. A nucleosome model (PDB 3LZ0) was docked into the densities and extranucleosomal DNA was manually built in UCSF ChimeraX and COOT (version 0.9). The H4 tail was built

### **Article**



using COOT (version 0.9). ADP·BeF $_3$  and a coordinated Mg $^{2+}$  ion was placed into the corresponding density by aligning PDB 509G to the closed state model in UCSF ChimeraX and docking the molecules into their corresponding density. Models were adjusted using ISOLDE (version 1.6) and in UCSF ChimeraX.  $^{64,65}$ 

Where the cryo-EM map resolution permitted, the model was inspected residue-by-residue using ISOLDE and refined to improve the fit to the map while maintaining favorable geometry. In places where our resolution approached 4.0 Å or worse (for example, most of CHD1 in the anchored and docked states), we limited the building process mainly to rigid-body docking of AlphaFold structures and resolving clashes. In the anchored and docked states, regions of ATPase lobe 2 were not visible due to heterogeneity, so ATPase lobe 2 docking was based on visible secondary structure, assuming a similar overall domain structure to that of the AlphaFold model. We were able to rigid-body dock CHD1 domains into the docked state (maps E–F) based on prominent secondary structure features but we did not deposit the docked state model to the PDB due to the limited resolution of CHD1 in maps E–F. Similarly, we were able to identify density corresponding to the DNA-binding region in maps G-I but were not confident enough to provide a pseudo-atomic model for these maps.

For the closed state, the complete model was real space refined in PHENIX<sup>63</sup> with one macro-cycle of global minimization, local rotamer fitting, morphing, simulated annealing, and ADP refinement with an overall weight of 0.5 and an ADP individual isotropic restraints weight of 0.5. For the anchored state, the complete models were real space refined in PHENIX<sup>63</sup> with one macro-cycle of global minimization and local grid search. Iterative rounds of manual rebuilding in ISOLDE together with real space refinement in PHENIX resulted in final models with good geometry.

### AlphaFold2 screen

To determine acidic patch interactions across chromatin remodeler families, we conducted an AlphaFold-Multimer screen<sup>70</sup> using *H. sapiens* histones H2A (Uniprot ID Q96QV6) and H2B (Uniprot ID P33778) with chromatin remodelers *H. sapiens* CHD2, CHD3, CHD4, CHD5, CHD6, CHD7, CHD8, CHD9, SMARCA1, SMARCA2, SMARCA4, and SMARCA5 as well as *S. cerevisiae* Isw1, Isw2, and Snf2. AlphaFold2-Multimer was run with standard parameters, generating a total of 10 predictions from 10 models. Highest rank models were selected and visualized.

#### Figure generation

Figures were generated using Adobe Illustrator, UCSF ChimeraX, and matplotlib.

### **QUANTIFICATION AND STATISTICAL ANALYSIS**

All fluorescence polarization experiments were analyzed with GraphPad Prism Version 10. Values were normalized by subtracting out the average background value for each set of replicates. Binding curves were fit with a sigmoidal binding equation:

$$y = \frac{x^{Hill \text{ slope}} * top}{x^{Hill \text{ slope} + EC_{50}}}$$

where x is the concentration of CHD1, top is the upper plateau of the fluorescence polarization values, Hill slope describes the steepness of the curve, and  $EC_{50}$  is the concentration of CHD1 that gives a response halfway between the zero and top. Because we are using nucleosome concentrations well below the dissociation constant ( $K_d$ ), we assume  $EC_{50}$  to be equal to the  $K_d$ . All experiments were conducted in triplicate and results are presented as individual data points and the mean  $\pm$  s.d. of three biologically independent experiments or samples as noted in figure legends.

For nucleosome sliding assays, rates were calculated based on the slope after fitting the first minute of the sliding reactions via linear regression and normalizing to the wild-type rate, and results are presented as individual data points and the mean  $\pm$  s.d. of three biologically independent experiments or samples as noted in figure legends.

### **ADDITIONAL RESOURCES**

We have no additional resources to describe.